Invited Research Article

Molybdenum isotope fractionation at upper-crustal magmatic-hydrothermal conditions

Anne K.C. Kaufmann[*], Thomas Pettke, Martin Wille

Institute of Geological Sciences, University of Bern, Baltzerstrasse 1+3, 3012 Bern, Switzerland

ARTICLE INFO

ABSTRACT

Molybdenum isotopes are an established proxy for paleoredox conditions in low-temperature surface systems. However, the mechanisms behind demonstrated Mo isotope fractionation during igneous and hydrothermal processes at elevated temperatures are still controversial. This study focusses on a comprehensive dataset documenting the late stage magmatic-hydrothermal evolution of Mo isotope systematics in miarolitic cavities and their host granite from a shallow arc-related intrusive system, the Torres del Paine laccolith in Chile. Molybdenum isotopic compositions ($\delta^{98}Mo_{SRM3134}$) were measured for (i) granitic bulk with or without petrographic signs of fluid loss, (ii) magmatic-hydrothermal fluids, and (iii) successively crystallised hydrothermal minerals and range from -1.6 to $+1.8$‰. The observed variability in $\delta^{98}Mo_{SRM3134}$ for individual miarolitic cavities approaching closed system conditions are smaller than the overall range in our dataset but still exceed 1.5‰. The Mo isotopic signature of magmatic fluids was directly measured for the first time by bulk dissolution of magmatic fluid inclusion bearing quartz. Absolute values for magmatic-hydrothermal fluids vary between $+0.6$ to $+1.8$‰ $\delta^{98}Mo_{SRM3134}$, which is significantly heavier than the granitic bulk rock signatures of -0.1 to $+0.46$‰ $\delta^{98}Mo_{SRM3134}$. Hydrothermal minerals in contrast exhibit variably light $\delta^{98}Mo_{SRM3134}$ between -1.6 and $+0.6$‰. Isotopic differences $\Delta^{98}Mo_{fluid\text{-}mineral}$ between fluid and hydrothermal minerals coexisting in the sampled cavities are largest for plagioclase with 1.9–2.2‰ $\Delta^{98}Mo$, and amount to 1.6–1.9‰ $\Delta^{98}Mo$ and 1.5–1.9‰ $\Delta^{98}Mo$ for alkali feldspar and biotite, respectively. Smaller values of 1.2–1.5‰ $\Delta^{98}Mo_{fluid\text{-}siderite}$, 0.8–1.9‰ $\Delta^{98}Mo_{fluid\text{-}molybdenite}$, 0.4–1.2‰ $\Delta^{98}Mo_{fluid\text{-}titanite}$ and 0.4–1.3‰ $\Delta^{98}Mo_{fluid\text{-}allanite}$ are obtained for higher Mo concentration minerals. Given that fluid-mineral pairs coexisted in equilibrium the ranges in $\Delta^{98}Mo_{fluid\text{-}mineral}$ values we report offer first constraints on the extent of hydrothermal Mo isotope fractionation. The magnitude and direction of these values agrees well with fractionation factors calculated based on an ionic bond-strength model for the incorporation of Mo^{6+} in hydrothermal minerals for crystallisation temperatures in miarolitic cavities (650–450 °C). This implies that significant fractionation effects can arise during hydrothermal processes even without changes in Mo redox state from oxidised fluids.

We can summarise the Mo isotope evolution during magmatic-hydrothermal processes as follows: First, Mo is transferred into the fluid phase exsolving from solidifying magma during late stage igneous evolution. The exsolved fluid subsequently precipitates hydrothermal minerals upon cooling, which dominantly incorporate light Mo isotopes (at variable $KD_{Mo}(fluid\text{-}mineral)$). With progressive hydrothermal crystallisation, the remaining fluid evolves to increasingly higher $\delta^{98}Mo_{SRM3134}$ along with decreasing Mo concentration.

Our data demonstrate that large variability in Mo isotopic signatures can be produced solely by primary magmatic-hydrothermal isotope fractionation processes at elevated temperatures. The generated large range in $\delta^{98}Mo$ signatures implies that (i) Mo isotopic signatures of evolved samples cannot be employed for tracing sources or precursor processes unless isotopic fractionation during magmatic-hydrothermal stages is quantified and can be corrected for; and (ii) mass balance models for the global Mo cycle used in paleoredox reconstruction need to account for potentially heterogeneous and isotopically fractionated continental contributions from evolved or hydrothermally overprinted rocks.

* Corresponding author.
E-mail addresses: akckaufmann@googlemail.com (A.K.C. Kaufmann), pettke@geo.unibe.ch (T. Pettke), martin.wille@geo.unibe.ch (M. Wille).

1. Introduction

The redox-dependent fractionation of molybdenum isotopes during low-temperature surface processes preserved in marine sediments is an important redox proxy that has been fundamental in constraining ocean paleoredox conditions and in tracing the oxygenation of the Earth's atmosphere (e.g., Anbar, 2004; Arnold et al., 2004; Siebert et al., 2006; Anbar et al., 2007; Wille et al., 2007; Dickson, 2017). These applications focus on changes in the global Mo mass balance and its sources – dominantly continental contributions by riverine transport (e.g., Archer and Vance, 2008) and to a lesser degree direct hydrothermal input (e.g., McManus et al., 2002) – and sinks, by exploiting the aqueous mobility of Mo^{6+} under oxidising conditions and characteristic isotopic fractionation during removal of Mo into reduced or oxidised sediments (e.g., Siebert et al., 2001; Nägler et al., 2005).

In contrast to the initial assumption of an isotopically homogeneous continental crust (e.g., Barling et al., 2001; Siebert et al., 2003), recent studies documented significant variations between 0.00 and 0.45‰ $\delta^{98}Mo_{SRM3134}$ for unaltered granites (Yang et al., 2017). Even larger variability is observed for igneous bulk rocks at collisional plate boundaries (e.g., Voegelin et al., 2014; Freymuth et al., 2015, 2016; König et al., 2016; Willbold et al., 2016; Willbold and Elliott, 2017; Gaschnig et al., 2017; Wille et al., 2018; Casalini et al., 2019; Chen et al., 2019; Villalobos-Orchard et al., 2020), suggesting that their Mo isotopic signatures are the result of complex geochemical processes.

Observed variability in mafic rocks from subduction zones was interpreted to result from direct recycling of an isotopically distinct slab input, the infiltration of an isotopically distinct, slab-derived fluid, characteristic mineral phases incorporating Mo into the overlying mantle wedge, or from a combination thereof (e.g., Freymuth et al., 2015, 2016; König et al., 2016; Willbold et al., 2016; Willbold and Elliott, 2017; Gaschnig et al., 2017; Casalini et al., 2019; Chen et al., 2019; Villalobos-Orchard et al., 2020). In these cases, additional fractionation of Mo isotopes during fractional crystallisation was not required to account for documented isotopic variability and therefore not considered to be relevant. This was supported by uniform Mo isotope ratios for a tholeiitic series of basalt to granite from Hekla volcano, Iceland (Yang et al., 2015). Molybdenum isotopic variability in hydrous, basaltic to andesitic arc rocks has therefore been proposed to represent a reliable tracer for different source inputs to arc magmas (e.g., Willbold and Elliott, 2017, and references therein).

In contrast to the tholeiitic series of Hekla, studies focusing on Mo isotope ratios during progressive igneous evolution in calc-alkaline systems reported an increase in measured $\delta^{98}Mo$ values with ongoing fractional crystallisation from olivine-basalt to dacite (e.g., Voegelin et al., 2014; Wille et al., 2018). In these systems, hydrous mineral separates, e.g., amphibole and biotite, preferentially incorporate light Mo isotopes; hence, cumulate formation may drive the remaining melt fraction towards heavier Mo isotopic compositions (Voegelin et al., 2014), although this interpretation has been challenged by mass balance calculations indicating that fractional crystallisation of hydrous minerals alone could not account for the shift in Mo isotopes alone (Willbold and Elliott, 2017). It was hypothesised that the measured Mo isotope fractionation between minerals and melts at elevated temperatures may be due to a change in Mo valence state from oxidised Mo^{6+} in melt to reduced Mo^{4+} in silicate minerals (Greber et al., 2014; Voegelin et al., 2014). However, other contributions favoured Mo^{6+} in silicate phases at redox conditions typical for most terrestrial geological settings (e.g., Hin et al., 2013, 2019; Willbold and Elliott, 2017, and references therein) and proposed that the preferred incorporation of light Mo into minerals arises from its higher (octahedral) coordination as opposed to a tetrahedral coordination (MoO_4^{2-}) in melts (e.g., Candela and Holland, 1984; Holzheid et al., 1994; O'Neill and Eggins, 2002; Farges et al., 2006; summarised in Willbold and Elliott, 2017).

Magmatic Mo isotope fractionation has not been observed for rocks with SiO_2 >68 wt% (Wille et al., 2018, and references therein),

interpreted to result from the fact that the dominant minerals crystallising during advanced fractional crystallisation are felsic and do not incorporate significant Mo (Voegelin et al., 2014). At higher SiO_2, a possible trend towards lighter bulk rock $\delta^{98}Mo$ might be related to the exsolution of a fluid phase that scavenges most heavy melt Mo (Greber et al., 2014), due to its fluid-mobile character with $KD_{Mo}(fluid\text{-}melt)$ on the order of 5–10 (Audétat and Pettke, 2003; Zajacz et al., 2008, and references therein). In summary, the different interpretations of the above studies indicate that the relevance of source variability versus magmatic fractionation to account for reported Mo isotope variability in igneous systems is still not well understood.

Molybdenum isotope data of hydrothermal molybdenite also reveal prominent variation in $\delta^{98}Mo$ (Hannah et al., 2007; Mathur et al., 2010; Greber et al., 2011; Greber et al., 2014; Shafiei et al., 2015; Breillat et al., 2016; Li et al., 2019; Chang et al., 2020). Several processes might be responsible for the large range in measured $\delta^{98}Mo$ in hydrothermal molybdenites, including prominent Mo source variability, fractionation of Mo isotopes by precipitation of molybdenite from hydrothermal fluids or during fluid phase separation into vapour and brine (Hannah et al., 2007; Greber et al., 2014; Shafiei et al., 2015; Li et al., 2019; Chang et al., 2020), potentially reflecting different Mo speciation in hydrothermal fluids (e.g., Ulrich and Mavrogenes, 2008; Rempel et al., 2009; Borg et al., 2012; Tattitch and Blundy, 2017).

The behaviour of Mo isotopes during hydrothermal processes can only be resolved with direct measurements of magmatic fluids and the coexisting hydrothermal minerals. However, magmatic-hydrothermal fluids have never been directly characterised in terms of Mo isotopic composition even though their significance for Mo transport, enrichment and, accordingly, isotopic fractionation has repeatedly been emphasised.

This study quantifies, by direct measurement of bulk rocks, minerals, and hydrothermal fluids from fluid inclusions, the progressive Mo isotope evolution of an evolved, subduction-related igneous system from magmatic-hydrothermal transition to purely hydrothermal stages as preserved in miarolitic cavities. We measured Mo concentrations and isotopic compositions by double spike MC-ICP-MS to identify characteristic signatures and systematics, as well as to determine fluid-mineral isotope fractionation factors for selected minerals in near-closed system miarolitic cavities. Our work offers hitherto unavailable data – including the first direct measurements of magmatic fluid $\delta^{98}Mo$ – to document the extent of Mo isotopic variability in magmatic-hydrothermal systems, with implications on continental crust-forming igneous systems. Our data offer clear perspectives on how to interpret Mo isotope variations measured at mineral to bulk rock to continental runoff scales.

2. Geology

The subduction-related Torres del Paine intrusive complex (TPIC) is one of several isolated intrusions to the East of the Patagonian batholith (Fig. 1, insert) in southern Chile (Michael, 1984; Ramírez de Arellano et al., 2012; Leuthold et al., 2013; Müntener et al., 2018; Ewing et al., 2018). Magmatic activity in this region is associated with the subduction of the Nazca and Antarctic plates beneath the South American plate.

The bimodal igneous complex intruded a series of gently folded Late-Cretaceous sediments (Michael, 1991; Wilson, 1991; Leuthold et al., 2013) at approximately 75–120 MPa corresponding to shallow crustal levels of about 2–3 km depth (e.g., Baumgartner et al., 2012; Leuthold et al., 2014), in discrete pulses between 12.59 and 12.43 Ma (Michel et al., 2008; Leuthold et al., 2012, 2013). The intrusion is fed by magma from a feeder zone in the west characterised by steep inter-magmatic contacts and extends as elongated laccolith eastwards (e.g., Leuthold et al., 2012, 2013). The felsic part of the laccolith consists of successive granitic magma pulses that assembled by underaccretion and are genetically related to the contemporary mafic rocks in the western Feeder Zone, while the underlying Paine Mafic Complex (PMC) formed later by internal overaccretion below the youngest Granite III. During
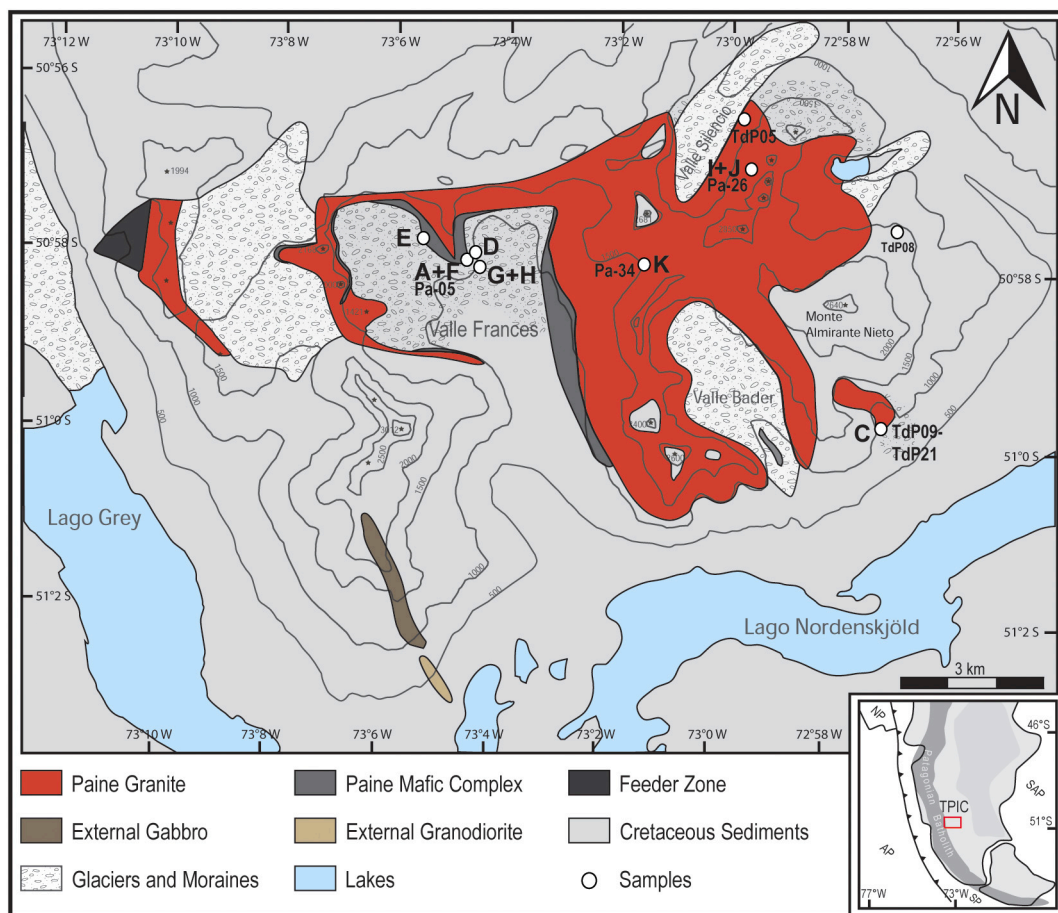
Fig. 1. Simplified geological map of the Torres del Paine igneous complex (TPIC) in Southern Patagonia (slightly modified after Baumgartner et al., 2012; Leuthold et al., 2013). The small insert shows the tectonic plate setting in South America (AP Antarctic plate, NP Nazca plate, SAP South American plate, SP Scotia plate), and the location of the TPIC. White markers indicate sampling sites for the miarolitic cavities (A-K) and bulk rock granite samples employed in this study. Positions of fallen blocks (see Table 1) indicate the sampling location only; a correlation with outcropping rock units cannot be inferred.

detailed studies, 3 granitic and 4 mafic units including hornblende-gabbros and monzodiorites were identified (Michel et al., 2008; Leuthold et al., 2012, 2013; Müntener et al., 2018). The three main granite units (with decreasing age) are named Almirante (Granite I), Fortaleza (Granite II), and Cathedral (Granite III) (Fig. 2). Each unit was constructed from numerous magma pulses that are internally divided by ductile contacts interpreted to represent emplacement of new magma batches in not fully solidified igneous host rocks; hence, such contacts
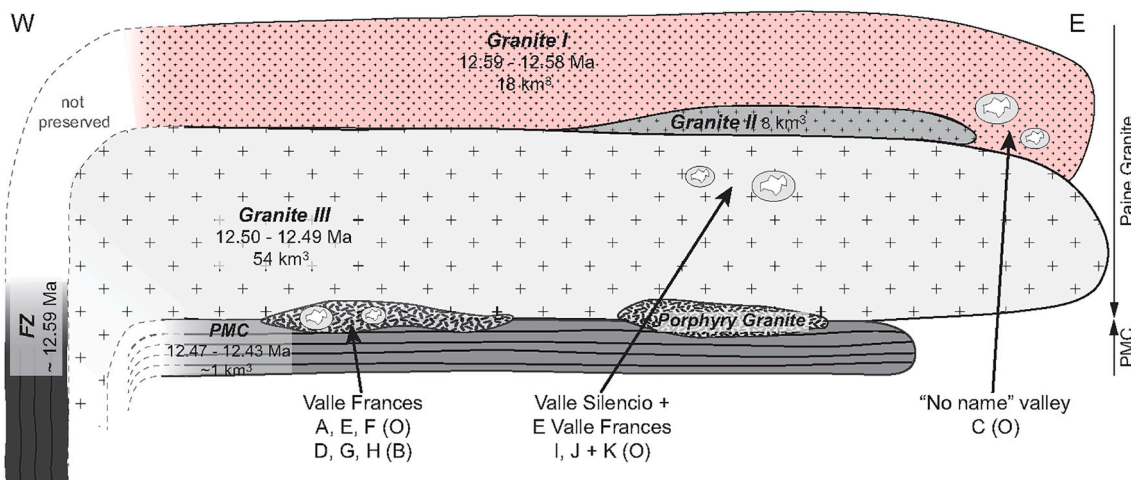
Fig. 2. Schematic profile drawing of the TPIC, illustrating the spatial and temporal relationships of the Paine Granite units and underlying Paine mafic complex (PMC), and the postulated relationship with the feeder zone (FZ) mafic rocks. The presence of sampled fluid exsolution features (miarolitic cavities) is visualised by small cavity symbols (not to scale). Arrows indicate conceptually which rock units are represented by the samples (grouped by sampling locations); O – sampled in outcrop; B – sampled in fallen block (units not inferred).

are commonly difficult to localise (e.g., Michael, 1984; Leuthold et al., 2013; Ewing et al., 2018).

The granite units represent highly fractionated rocks (SiO$_2$ ranging from 73 to 78 wt%) of an arc-related magma possessing a mantle source with a dominant subduction component and insignificant crustal assimilation (Leuthold et al., 2013). They were interpreted as felsic crystal mush with highly evolved interstitial liquid (Michael, 1984), which underwent local fluid exsolution at volatile (mainly H$_2$O) saturation as documented by distinct fluid exsolution features, including miarolitic cavities and localised zones of vuggy textures. These features are concentrated in a few outcrop areas in the different granite units, supporting that fluid exsolution occurred localised and very late during the igneous evolution under constant confining pressure. The amount of low-density fluid released upon fluid saturation was too small to achieve the overpressure necessary to rupture the prominently crystallised mush. Therefore, isolated cavities preserved "bubbles" of exsolved volatiles in the solidifying magma, allowing for protracted magmatic-hydrothermal crystallisation under near closed-system conditions.

2.1. Samples

For this study, we sampled granitic bulk rocks documenting the process of cavity formation, as well as hydrothermal minerals that precipitated from magma-derived fluid in miarolitic cavities (Fig. 3,4,5; Table 1).

Miarolitic cavities in the TPIC are isolated features, i.e., not interconnected, and range in size from few mm to one metre. They are often surrounded by a few mm to ca. 5 cm wide transition zone exhibiting graphic intergrowth of quartz and feldspar, indicating eutectic crystallisation upon fluid exsolution. These small-scale near-closed systems record the complete magmatic-hydrothermal evolution from ~650 down to <300 °C as demonstrated by occasional presence of zeolites.

We sampled cavity-rich zones in Valle Frances, Valle Silencio, and a small valley ("No name") south of Mt. Almirante Nieto (Fig. 1, Table 1). The sample sequence selected for this study encompasses bulk rocks hosting the cavities, specifically (i) granites without signs of fluid saturation, simply labelled "granite", (ii) the narrow leucocratic transition zone directly surrounding the cavities that is often characterised by graphic texture, (iii) miarolitic granites with small-scale (mm – cm) fluid exsolution textures, and (iv) fine-grained aplite (labelled as Ap). Bulk rock samples of groups (ii) and (iii) displaying textural evidence for fluid exsolution are distinguished from granites without signs of fluid

saturation (i) with the label FF (standing for fluid features).

No name-valley samples (C') are associated with the oldest Granite I (Almirante), and comprise a selection of bulk rock samples including granite and graphic granite, as well as one >50 cm cavity (C). In Valle Silencio, samples comprise one granite and an associated cavity (I), two additional cavity samples in close spatial relation to I (J, K) and another granite sample (TdP05) exposed at lower elevation, close to the contact with the metasediments. Samples from Valle Frances make up the largest group of cavity samples (A, D, E, F, G, H, K). For cavity A, a corresponding transition zone bulk rock sample (Pa-05(FF)) is available. Outcrop samples (A, E, F) are associated with the Porphyritic Granite, likely representing the youngest granite unit, observed at the boundary of lowermost granite and the underlying PMC (Fig. 2). Accordingly, these represent comparatively higher temperatures and somewhat lower degrees of fractionation upon fluid exsolution, which is reflected in the more complex hydrothermal mineralogy of the cavities. Cavity K sampled on the eastern side of the valley closely resembles the samples from upper Valle Silencio. Note that the associated granite units for sampled cavities in fallen blocks (D, G, H from Valle Frances, TdP08 on Almirante Nieto) cannot be identified unequivocally.

Bulk rock samples are fine- to medium-grained granites consisting of quartz, albite-rich plagioclase, alkali feldspar, and biotite. They encompass highly fractionated granite (73–77 wt% SiO$_2$, see Table A1.1) and are thus representative of the evolved part of the TPIC suite as documented by Michael (1984), Leuthold et al. (2013), and Müntener et al. (2018).

Characteristic fluid mobile (Zn, Cs, and Ba) and immobile (Ta, Th) trace element data (Table A1.1) indicate that the bulk rock samples document variable degrees of fluid loss during the late stage magmatic evolution of the TPIC, which is most pronounced for the samples with visible fluid features (compare Fig. A2.1). Depending on the evolution of the igneous system, fluid phase saturation and exsolution can occur at variable crystallinity of the magma. While it is possible that the magma lost some fluid already prior to laccolith emplacement, the miarolitic cavities sampled here document moderate fluid exsolution that occurred in a crystal mush of the laccolith (i.e., at variably high magma crystallinity), probably induced by progressive crystallisation of dominantly anhydrous minerals (e.g. Candela, 1997). The amount of fluid exsolved at this stage was likely moderate, thus facilitating the preservation of isolated fluid filled cavities as opposed to interconnected fluid escape pathways. Consequently, the cavities can be taken as representative of late stage fluid exsolution in evolved continental arc magmas at shallow
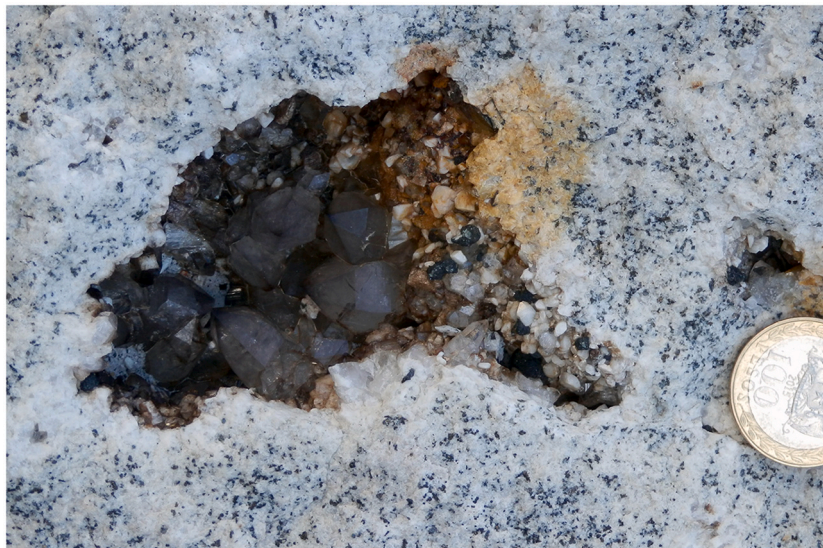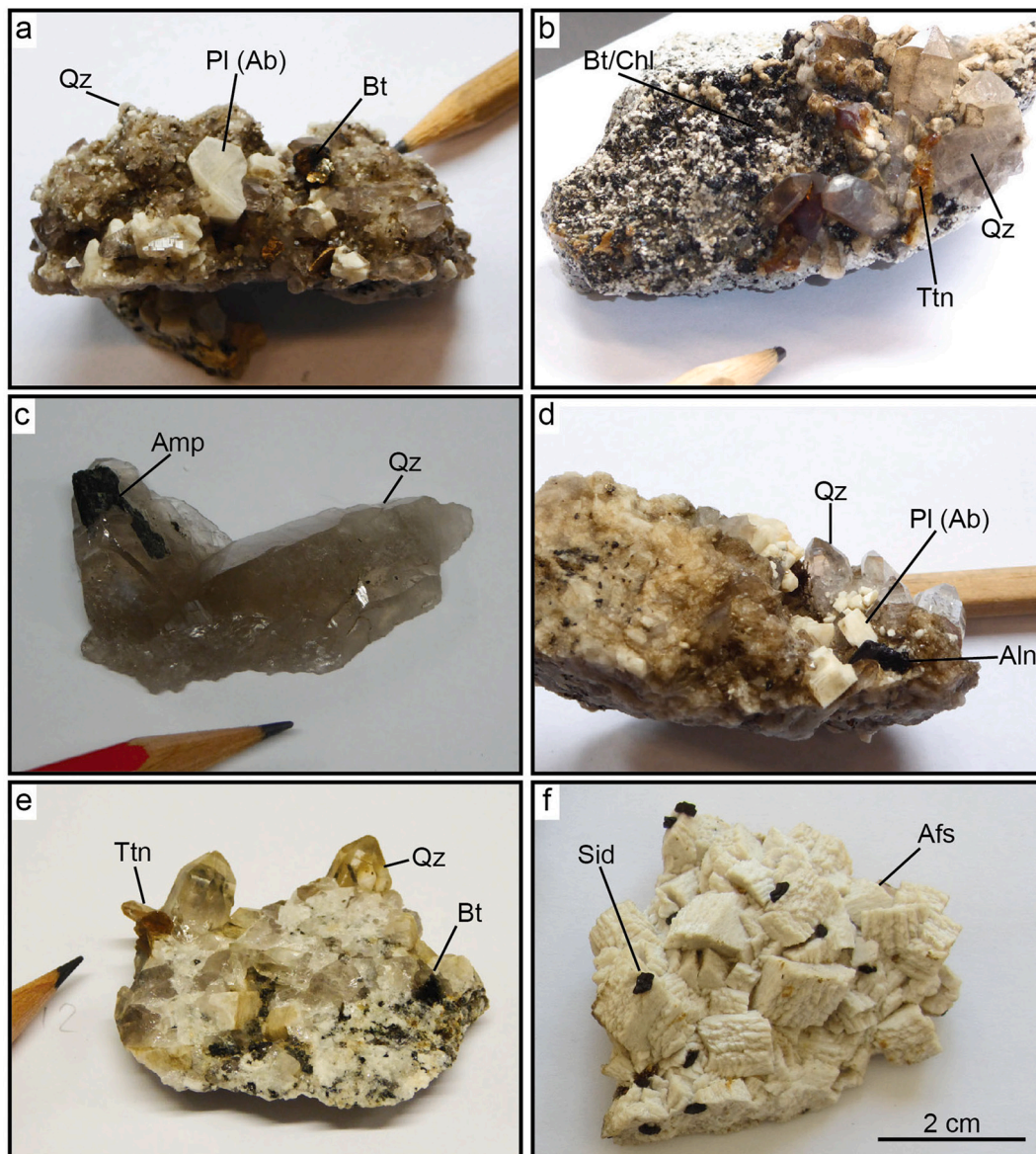

Fig. 3. shows an example of a miarolitic cavity in granitic host rock from Valle Frances, exhibiting the typical leucocratic transition zone rich in feldspar and quartz along the lower cavity rim.

Fig. 4. Examples of hand specimens showing the various hydrothermal minerals lining miarolitic cavity walls: a: cavity A, b: cavity H, c: cavity D, d: cavity A, e: cavity H, f: cavity C. Mineral abbreviations after Whitney and Evans (2010).

crustal depth, interpreted as sources of ore-forming magmatic-hydrothermal fluids (e.g. Audétat et al., 2008).

### 2.2. Mineralogy of the miarolitic cavities

A transition zone of graphic intergrowth of quartz and feldspar often forms a boundary layer between granite and the open cavity (Fig. 3 and 5). For the purpose of this work, all minerals growing from this eutectic graphic texture zone into the open cavity will be defined as hydrothermal phases that precipitated from the cavity forming magmatic-hydrothermal aqueous fluid.

The cavity walls are lined with free-grown crystals (Fig. 3, 4, 5) in variable proportions as a function of the immediate host rock. They comprise dominantly quartz, with additional plagioclase, alkali feldspar, biotite, ±amphibole, ±titanite, and ±allanite. In few cavities, some late siderite, and very rarely molybdenite or fluorite was observed. In detail, cavity C is characterised by a simple mineralogy of quartz, alkali feldspar and late stage siderite. Similarly, cavity I characterised by quartz, alkali feldspar and slightly chloritised biotite, and cavities J and K containing quartz, feldspar, and ±allanite are characterised by simple

mineralogy. Some cavities most likely associated with the Porphyry Granite often contain also titanite (D, E, H), sometimes allanite or rarely epidote (A, D), amphibole (D, E), and in one case molybdenite (D) in addition to the dominant quartz, feldspars, and ± biotite (see Table 1). Mineral identification in the hand specimens has been confirmed with Raman spectroscopy where uncertain (exemplary spectra are presented in Fig. A2.2 and A2.3).

Based on the observations of growth relationships and positions in the hand samples and thick sections, we can infer a crystallisation sequence compiled from all cavities (Fig. 5). Quartz is present continuously from the eutectic zone until late hydrothermal stages. Alkali feldspar and Ab-rich plagioclase tend to be magmatic to early hydrothermal. Biotite and amphibole can occur during all high temperature stages, but they rarely coexist in the same cavity and their growth phase relative to other minerals differs slightly between cavities. Chlorite can be observed as late alteration product in a few cavities, mostly after biotite. Allanite occurs as individual crystals growing in contact with the eutectic zone, but without any direct growth relationships we cannot define the exact relative timing with respect to the other minerals. Nonetheless, its position and idiomorphic habitus testify to
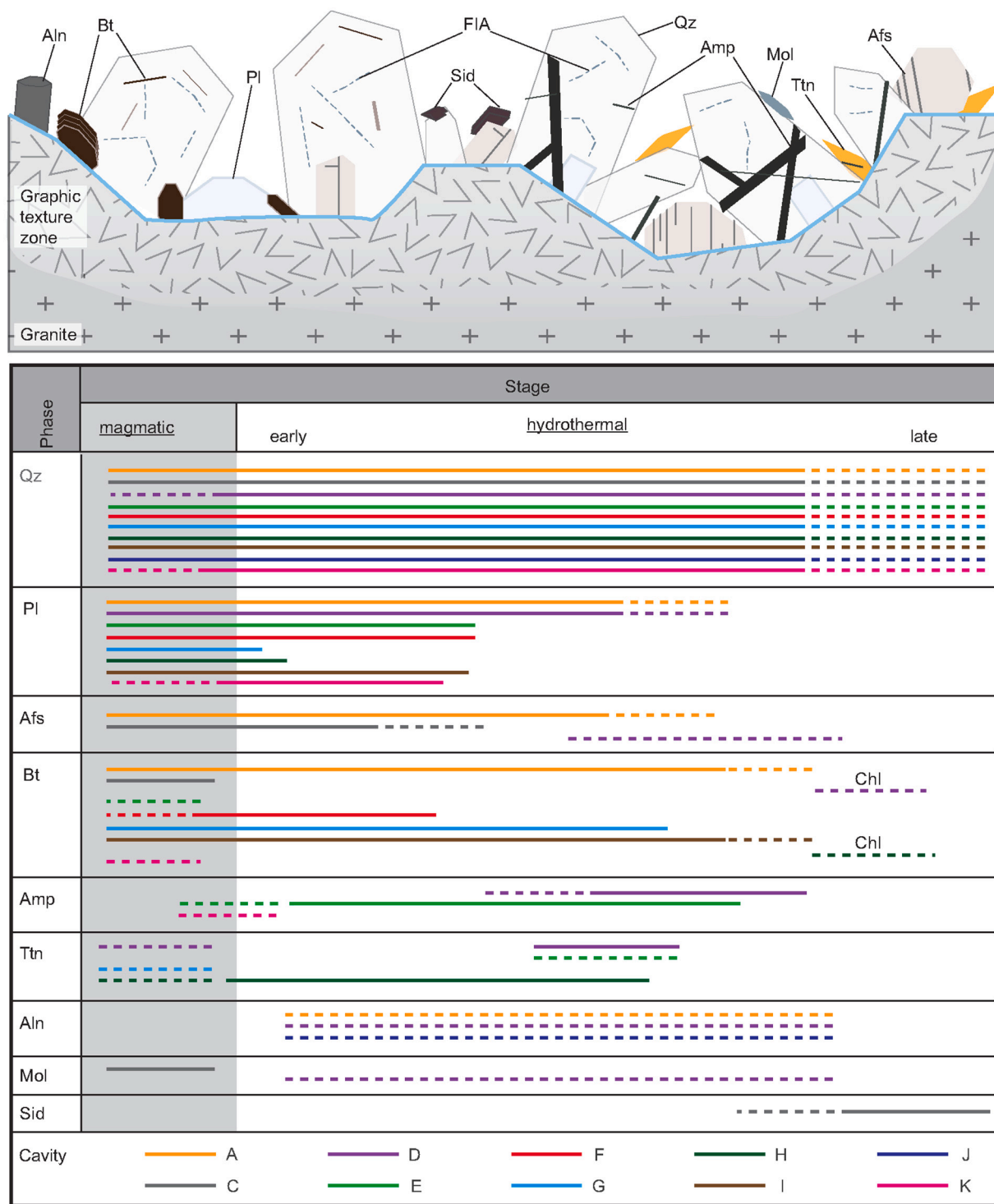
Fig. 5. Top: Schematic drawing representing the growth relationships of phases associated with miarolitic cavities investigated for Mo isotopic fractionation effects. The blue line outlining the cavity wall indicates the transition from the magmatic to the hydrothermally dominated regime. FIA stands for fluid inclusion assemblage and refers to a set of cogenetic inclusions entrapped together in a host crystal; Bottom: Crystallisation sequence determined for the minerals preserved in the cavities inferred from observed growth relationships and positions in hand specimens. Mineral abbreviations according to Whitney and Evans (2010). (For interpretation of the references to colour in this figure legend, the reader is referred to the web version of this article.)

hydrothermal growth into open space. Titanite and siderite are often observed growing on free-grown quartz and feldspar crystals, indicating a comparatively late growth. This is further confirmed by the inclusion of amphibole needles in titanite. Rare free-grown molybdenite crystals could only be observed in cavity D in the loose cavity-filling material; hence, no intergrowth relationship with other phases could be

established that could further constrain the timing of molybdenite precipitation. Quartz crystals in the granite and in the graphic texture zone were found to sometimes incorporate small molybdenite inclusions (as can often be observed in felsic rocks; Audétat et al., 2011), attesting to molybdenite saturation already at late magmatic stages (Fig. A2.4).

Inclusions in eutectic magmatic quartz and in hydrothermal cavity

Table 1
List of sampling locations for bulk rocks and cavity samples at Torres del Paine. Mineral abbreviations following Whitney and Evans (2010).

Cavity	Sample	Location	S	W	Elevation (m)	Unit[+]	Cavity mineral assemblage	Associated rock samples + lithology
A	Pa-05	Frances	50°57.995'	73°04.610'	1080	Porphyry Granite	Qz + Afs + Pl + Bt + All	Pa-05(FF) - leucocratic transition zone
C	TdP17–21	No name	50°59.734'	72°57.089'	881	I (Almirante)	Qz + Afs ± Bt + Sid	TdP12, TdP13, TdP15a(L)[b] - granite; TdP15a(D)[b] - Bt-granite; TdP09(FF) - miarolitic granite; TdP14(FF), TdP21(FF) - graphic granite
D	Pa-17	Frances	50°57.904'	73°04.460'	960	Block	Qz + Pl + Amp + Ttn + All/Ep + Mol (+Cal)	
E	Pa-10	Frances	50°57.768'	73°05.402'	1200	Porphyry Granite	Qz + Amp + Ttn	
F	Pa-04	Frances	50°57.995'	73°04.610'	1080	Porphyry Granite	Qz + Bt (+ Stb)	
G	Pa-13	Frances	50°58.071'	73°04.372'	950	Block	Qz + Bt	
H	Pa-12	Frances	50°58.071'	73°04.372'	950	Block	Qz + Ttn	
I	Pa-26	Silencio	50°56.812'	72°59.601'	1716	III (Catedral)?	Qz + Afs + Bt	Pa-26 - Bt-granite
J	Pa-25	Silencio	50°56.812'	72°59.601'	1716	III (Catedral)?	Qz + All	
K	Pa-33	Frances	50°57.960'	73°01.443'	1544	III (Catedral)?	Qz + Pl	
–	TdP08	Almirante Nieto	50°57.446'	72°57.047'	1427	block	Qz + Afs + Sid	
–	TdP05*[a]	Silencio	50°56.239'	72°59.767'	ca. 1092	I (Almirante)?	no cavity	TdP05 - granite
–	Pa-34[a]	Frances	–	–	–	I (Almirante)?	no cavity	Pa-34(Ap) - aplite

+ Association with granite units as determined from sample location.
* Coordinates 50 m above sampling location.
[a] No cavity samples associated with these bulk rock samples.
[b] TdP15a consists of a Bt-poor part (L) and Bt-rich part (D).

quartz document coexisting brine, vapour, and silicate melt at Torres del Paine. This is consistent with the fluid phase states in the binary H_2O-NaCl system (e.g., Driesner and Heinrich, 2007) at P and T of granite emplacement and subsequent hydrothermal cavity evolution (~650 °C down to <300 °C at ≤120 MPa). The fluid inclusions exhibit Mo concentrations from <1 to several tens of µg/g, with higher concentrations typically observed for brines and lower for vapour-rich fluid (see Table A1.2).

3. Methods

3.1. Raman spectroscopy

First order identification of hydrothermal cavity minerals – including checking for the presence of carbonate phases before sample cleaning with acids – was done by Raman spectroscopy, employing a confocal Jobin Yvon Horiba microprobe (LABRAM HR-800) connected to an Olympus BX41 microscope equipped with multiple objectives from 4× to 100× magnification. Both 532 nm and 633 nm lasers were used to achieve best spectra (low fluorescence) for all phases. The 521 cm^{-1} Raman band of silicon was used to calibrate the spectrometer before each measurement session.

3.2. Sample preparation and cleaning

All bulk rock sample comminution steps were done in a metal free (i. e., agate), clean environment to avoid Mo contamination from metal alloys. Hence, saw-cut surfaces of large rock pieces were chipped off and discarded. Splitting of rock fragments was done in a purpose-designed press to produce ≤ cm sized pieces, further crushed with a petrological hammer while being wrapped in several layers of plastic bags.

Cavity mineral samples were cleaned from surface dirt using a high-pressure water cleaner followed by immersion in an oxalic acid bath (only carbonate-free samples) to remove clay residues without attacking the silicate minerals, followed by repetitive ultrasonication in distilled water for acid neutralisation. Mineral separates (compare Fig. A2.5) were carefully hand-picked under a binocular microscope to avoid contamination by inclusions or surface overgrowth. Larger crystals were crushed in an agate mortar to optimise the surface to volume ratio for acid digestion. Prior to digestion, mineral separates were repeatedly ultrasonicated again in ultrapure water (MilliQ).

Inclusion bearing quartz was cut into slices with a conventional diamond saw. Pieces were then inspected using a binocular microscope for fluid inclusion content (employing immersion oil) and to avoid mineral inclusions and possible melt inclusions. If impurities or solid inclusions were detected, these were removed by further cutting. If this was not feasible, affected sample chips were discarded. Selected pieces for fluid data and one control sample containing melt inclusions were then thoroughly surface-cleaned by repetitive bathing in acetone to remove oil residue, followed by ultrasonicating in ethanol to remove remains of acetone, and finally in distilled water. A final surface cleaning step in 1–2 M *aqua regia* was performed under clean lab conditions for approximately 30 min at room temperature to completely remove any potential metal contamination without risking an effect on the inclusion contents by diffusion (see section 3.4 and Appendix B).

3.3. LA-ICP-MS

Major element, Mo, and REE (in case of allanite/epidote) concentrations of hydrothermal minerals were obtained by laser ablation-inductively coupled plasma-mass spectrometry (LA-ICP-MS) at the University of Bern. The LA-ICP-MS system employed consists of a Geolas Pro 193 nm ArF Excimer laser (Lambda Physik, Germany) coupled with an ELAN DRCe quadrupole mass spectrometer (QMS; Perkin Elmer, USA). Details on the setup and optimisation strategies can be found in Pettke et al. (2012). The analytical set-up was tuned daily for optimum

performance across the entire mass range, to satisfy a ThO production rate of below 0.2% (i.e., Th/ThO intensity ratio <0.002), and to achieve robust plasma conditions monitored by a Th/U sensitivity ratio of 1 as determined on the SRM612 glass standard. Measurements were done using 10 Hz laser repetition rate and 60–120 μm beam sizes, choosing the maximum possible to minimise limits of detection. Molybdenum was recorded on ^{95}Mo, ^{97}Mo, ^{98}Mo, ^{100}Mo in order to monitor whether a given mass suffers from polyatomic metal-argide interferences. External standardisation was done employing GSD-1G from USGS and SRM612 from NIST was measured for quality control. Internal standardisation employed the sum of major element oxides, minus stoichiometric water for hydrous minerals. Data reduction was done off-line using the SILLS program (Guillong et al., 2008), with rigorous limits of detections calculated for each element in every analysis following the formulation detailed in Pettke et al. (2012). The obtained Mo concentrations were mainly used to determine appropriate sample size and corresponding spike weight for Mo isotope ratio determination.

3.4. Sample digestion and Mo isotope analysis by double spike MC-ICP-MS

Samples were weighed in into Savillex Teflon beakers according to their Mo concentrations, targeting 100 ng Mo for bulk rocks, 25–50 ng Mo for mineral separates, and ideally ≥20 ng for bulk quartz fluid inclusions (corresponding to between 1 and 3 g of quartz). A combination of HNO_3, HF, and HCl was used to digest the samples (Wille et al., 2007) depending on the sample matrix (e.g., silicates, carbonates, or sulphides). In order to determine Mo isotopic composition as well as concentrations, a ^{97}Mo-^{100}Mo double spike was added aiming for a spike to sample ratio of 1 (Siebert et al., 2001; Rudge et al., 2009; John, 2012). Molybdenum isolation was done in a 2-step ion chromatography procedure using first 1.5 ml (or 2 ml for batches including Fe-rich samples) of Dowex 1 × 8 (200–400 mesh) anion resin, followed by Dowex 50WX8 (200–400 mesh) resin for cation exchange. A detailed documentation of the sample preparation and ion chromatography is given in Appendix B1, with detailed procedures provided in Table B1.2.1. An assessment of the bulk quartz dissolution method in terms of potential contamination with solid inclusions is provided in Appendix B2.

Molybdenum isotope measurements were performed at the Institute of Geological Sciences, University of Bern on a Neptune Plus multi-collector ICP-MS (Thermo Fisher Scientific) employing an Aridus II (Teledyne CETAC) desolvating sample introduction system. The measurements were conducted in low resolution mode using Ni skimmer (X) and standard sample cones. Molybdenum was measured on masses 94, 95, 96, 97, 98, and 100, and masses 99 and 101 were recorded to account for potential Ru interferences on ^{96}Mo, ^{98}Mo, and ^{100}Mo. On each measurement day the system was routinely tuned for optimal conditions such as a stable signal and high signal to background ratio, and a flat, centred peak for all masses by adjusting gas flows, torch position and lens settings. Signal intensity on ^{96}Mo was generally between 2 and 4 V for 25 ppb standard solutions. Procedural blanks for the digestion and Mo isolation processes contained in general between 0.57 and 0.95 ng Mo, with the lowest values (0.57 and 0.61 ng) for the bulk quartz dissolution blanks.

A measurement sequence consisted of alternating sample and background (on peak zero) measurements on pure 0.5 M HNO_3 carrier solution, with 60–80 and 30 cycles, respectively, with a signal integration time of 4.194 s per cycle. Standard solutions of the National Institute of Standards and Technology (NIST) SRM3134 (LOT 891307) and Johnson Matthey Mo ICPMS calibration standard JMCBern (LOT 602332B) were measured repeatedly during each session to monitor analytical precision and accuracy.

Data were reduced to obtain Mo isotopic compositions as well as concentrations following the principles described in Siebert et al. (2001). Molybdenum isotopic compositions are expressed using the conventional δ notation relative to the NIST SRM3134 reference

material (Greber et al., 2012; Goldberg et al., 2013):

$$\delta^{98}Mo_{SRM3134}[‰] = \frac{\left(\frac{^{98}Mo}{^{95}Mo}\right)_{sample} - \left(\frac{^{98}Mo}{^{95}Mo}\right)_{SRM3134}}{\left(\frac{^{98}Mo}{^{95}Mo}\right)_{SRM3134}} \cdot 1000 \quad (1)$$

Isotopic differences between two coexisting phases A and B with measured isotopic signatures $\delta^{98}Mo_A$ and $\delta^{98}Mo_B$ are calculated as follows:

$$\Delta^{98}Mo_{A-B}[‰] = \delta^{98}Mo_A - \delta^{98}Mo_B \quad (2)$$

Given that the phases A and B coexisted at equilibrium, the isotopic fractionation factor α between these two phases A and B is defined as

$$\alpha_{A-B} = \frac{\left(\frac{^{98}Mo}{^{95}Mo}\right)_A}{\left(\frac{^{98}Mo}{^{95}Mo}\right)_B} \quad (3)$$

This relates to the isotopic fractionation ε as follows:

$$\varepsilon_{A-B}[‰] = 1000 \cdot ln\alpha_{A-B} \quad (4)$$

For two phases that coexisted in equilibrium, this corresponds to the measured isotopic difference $\Delta^{98}Mo$ (in ‰) (see e.g., Coplen, 2011).

The external reproducibility of Mo isotope data was determined from repetitive measurements of JMCBern, and measurement accuracy was determined by measuring USGS rock reference materials. The value of JMCBern relative to NIST3134 averaged over all these sessions is −0.26 ± 0.03 (2SD) ‰ $\delta^{98}Mo$, which is in very good agreement with previously published values (e.g., Greber et al., 2012; Goldberg et al., 2013). USGS reference materials AGV-2, GSP-2, RGM-2, and BIR-1a processed together with the samples (see Table 2) agree within error with published values if available (AGV-2: Willbold et al., 2016; GSP-2: Yang et al., 2015; BIR: Burkhardt et al., 2014), indicating a 2SD external reproducibility of 0.08‰ for samples with concentrations of a few ppm Mo, and ca. 0.11‰ for samples with <1 ppm Mo (BIR). Molybdenum concentration measurements by isotope dilution (ID) MC-ICP-MS are accurate to within ±2% uncertainty (see Greber et al., 2012).

3.5. Modelling of Mo isotope fractionation

We modelled force constants and corresponding isotopic fractionation (expressed as $\varepsilon^{98}Mo_{A-B}$ [‰] = 1000 $ln\alpha_{A-B}$) as a function of temperature according to Young et al. (2015, their equations 31 and 29, respectively). The calculation takes into account valence states of cations and anions in corresponding molecules and the average ionic distance (bond length) for a given coordination. We employed known structural information to calculate fractionation factors for molybdate, Mo-oxides, and molybdenite as provided in Table B3.1 (Appendix B3).

For Ti-bearing minerals, available structural information on Ti incorporation in titanite, biotite, and amphibole was used as approximation for Mo, assuming substitution in the same structural position due to the similar ionic radii (e.g., Shannon, 1976; Zack et al., 2002). Additional effects of minimally different ionic radii and therefore bond length might occur, but without independent constraints this parameter is kept constant, using literature data for the Ti octahedron in titanite (Kunz et al., 1996) and the M2 site in biotite and amphibole, which is typically occupied by Ti (Hawthorne and Oberti, 2007; Chukanov et al., 2008), given in Table B3.2 (Appendix B3). For comparison, we always calculated fractionation factors for the two common Mo valence states (4+ and 6+).

4. Results

Molybdenum concentrations ([Mo]) determined by LA-ICP-MS and

Table 2

Molybdenum concentrations and isotope compositions of bulk rocks, fluids, and minerals. Sample repeats (different dry splits of bulk rock powders or mineral separates) are indicated by consecutive numbers at the end of the sample name.

Cavity	Sample	Phase[+]	Mo (LA)		Mo (ID)[a]	$\delta^{98}Mo_{SRM3134}$	
			μg/g	SD[b]	μg/g	‰	2SE[c]
A	Pa-05(FF)_1	Bulk rock	0.10	0.08	0.08	0.31	0.02
A	Pa-05(FF)_3	Bulk rock	"	"	0.09	0.26	0.03
A	Pa-05(All)	Allanite	0.03	0.01	0.11	0.20	0.12
A	Pa-05(Bt)	Biotite			1.64	−1.01	0.02
A	Pa-05(Plag)_1	Plagioclase			0.03	−1.06	0.03
A	Pa-05(Plag)_2	Plagioclase	0.02	0.004	0.06	−1.56	0.02
A	Pa-05(Ksp)	Alkali feldspar			0.04	−0.73	0.02
A	Pa-05(Qz-MI)	Melt			*0.013*	0.30	0.02
C'	TdP09(FF)	Bulk rock	0.49	0.11	0.76	0.04	0.01
C'	TdP12	Bulk rock	2.39	0.88	2.33	0.08	0.01
C'	TdP13_1	Bulk rock	1.08	0.42	2.81	0.26	0.01
C'	TdP13_2	Bulk rock	"	"	1.85	0.16	0.01
C'	TdP13_3	Bulk rock	"	"	1.76	0.09	0.02
C'	TdP15a(L)**	Bulk rock	0.85	0.14	1.72	0.23	0.01
C'	TdP15a(D)**	Bulk rock	2.01	0.31	3.91	0.16	0.02
C'	TdP14(FF)	Bulk rock	0.69	0.16	0.81	0.06	0.01
C'	TdP21(FF)_1	Bulk rock	0.30	0.03	0.36	0.10	0.01
C'	TdP21(FF)_3	Bulk rock	"	"	0.43	0.04	0.02
C	TdP19(Ksp)	Alkali feldspar	0.02	0.003	0.03	−0.19	0.02
C	TdP19(Sid)	Siderite	28	13.7	35	0.22	0.02
D	Pa-17(Ti)_2	Titanite	4.40	0.78	9.83	0.25	0.02
D	Pa-17(Am) (n = 7)	Amphibole	0.04	0.01	0.02–0.19		
D	Pa-17(Plag)	Plagioclase	0.08	0.06	0.02	−0.17	0.02
D	Pa-17(Cc)	Calcite			0.002		
D	Pa-17(Mo1)	Molybdenite			~60 wt%	−0.21	0.01
D	Pa-17(Mo2)	Molybdenite			~60 wt%	−0.24	0.01
D	Pa-17(Qz-FI)	Fluid			*0.003*	1.50	0.04
E	Pa-10(Ti)_2	Titanite			5.42	0.49	0.02
E	Pa-10(Ti)_3	Titanite			5.21	0.56	0.02
E	Pa-10(Am) (n = 6)	Amphibole	0.05	0.01	0.01–0.05		
E	Pa-10(Qz-FI)_3	Fluid			*0.012*	1.73	0.03
E	Pa-10(Qz-FI)_4	Fluid			*0.009*	1.55	0.03
F	Pa-04(Bt)_1	Biotite	1.40	0.44	2.89	−1.28	0.01
F	Pa-04(Bt)_2	Biotite	"	"	3.12	−1.17	0.01
F	Pa-04(Qz-FI)	Fluid			*0.006*	1.17	0.04
G	Pa-13(Bt)_1	Biotite (chl?)			0.65	−0.27	0.02
G	Pa-13(Bt)_2	Biotite (chl?)			0.64	0.26	0.02
G	Pa-13(Qz-FI)	Fluid			*0.008*	1.23	0.03
H	Pa-12(Ti)_1	Titanite	2.45	0.57	27.0	0.37	0.03
H	Pa-12(Ti)_2	Titanite	6.16	0.18	23.2	0.38	0.03
I	Pa-26	Bulk rock	0.57	0.03	1.20	−0.08	0.01
I	Pa-26(Bt)	Biotite-chlorite			1.55	−1.06	0.02
I	Pa-26(Fsp)	Alkali feldspar	0.05	0.03	0.08	−0.96	0.02
I	Pa-26(Qz-FI)	Fluid			*0.043*	0.61	0.02
J	Pa-25_All_1	Allanite			2.52	0.38	0.07
J	Pa-25(All)_2	Allanite	1.85	0.97	3.49	0.21	0.02
J	Pa-25(All)_3	Allanite			3.60	0.28	0.02
J	Pa-25(Qz-FI)	Fluid			*0.006*	0.79	0.03
K	Pa-33(Plag)	Plagioclase	0.03	0.02	0.04	−0.14	0.02
K	Pa-33(Qz-FI)	Fluid			*0.055*	0.92	0.03
–	TdP05	Bulk rock	2.36	0.31	2.29	0.14	0.03
–	Pa-34(Ap)	Bulk rock	1.30	0.09	1.57	0.46	0.01
–	TdP08(Sid)	Siderite	260	150	477	−0.63	0.02
Reference materials							
AGV-2 av. (N = 4)*		Andesite			1.96	−0.16	0.07
BIR (N = 2)*		Basalt			0.04	−0.16	0.11
GSP-2 av. (N = 2)*		Granodiorite			2.24	−0.24	0.08
RGM-2 (N = 1)*		Rhyolite			2.36	0.12	0.01

LA stands for LA-ICP-MS. ID stands for isotope dilution MC-ICP-MS. Mo concentrations with uncertainties estimated at 2%.

FI and MI stand for fluid inclusions or melt inclusions, respectively, in quartz.

[+] Phase refers to bulk rock, hydrothermal fluid, or hydrothermal minerals as specified.

[a] Fluid concentration values are set in italics because they represent the apparent bulk quartz Mo concentrations.

[b] SD calculated from individual spot measurements per mineral or pressed powder pellet (PPP, N = 6).

[c] SE calculated from all measurement cycles after outliers outside the 95% confidence interval were removed.

[*] Uncertainty for repeated measurements of reference material (N in bracket) given as 2SD.

[**] TdP15a(L): leucocratic, Bt-poor part of the bulk rock sample, TdP15a(D): Bt-rich, darker part of the bulk rock sample.
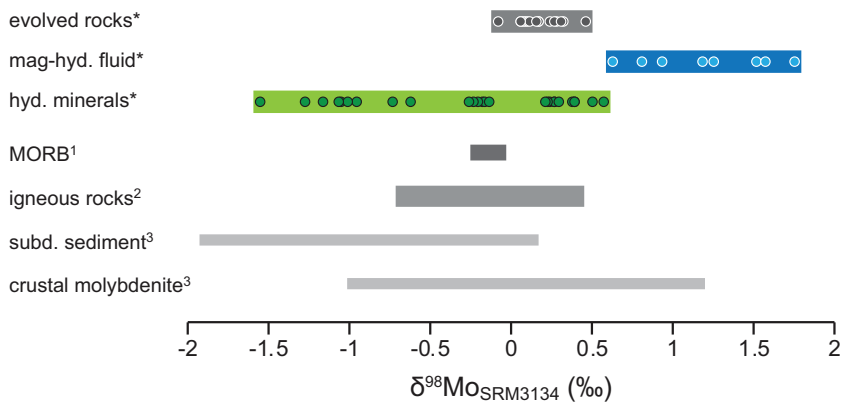
Fig. 6. Ranges of Mo isotopic signatures measured for the magmatic-hydrothermal sample suite in the present study (*) including evolved rocks, aqueous fluid and hydrothermal minerals, in comparison to published data for: 1: pristine MORB (Bezard et al., 2016); 2: signatures of igneous rocks compiled from Greber et al. (2014), Voegelin et al. (2014), Yang et al. (2015), Freymuth et al. (2015, 2016), König et al. (2016), Gaschnig et al. (2017), Yang et al. (2017), Wille et al. (2018), Casalini et al. (2019), and Villalobos-Orchard et al. (2020); 3: compilation of data for subducted sediments and molybdenites from Willbold and Elliott (2017).

isotope dilution MC-ICP-MS, as well as isotopic compositions for all phases are summarised in Table 2 and illustrated in Fig. 6. Additional LA-ICP-MS major element and REE concentration data for exemplary hydrothermal minerals are presented in supplementary Table C.1 (Appendix C).

At variable concentrations in bulk rocks (0.08–3.91 μg/g Mo), magma-derived fluid (<1 – several tens of μg/g Mo), and hydrothermal minerals (from 0.03 μg/g in alkali feldspar up to 60 wt% in molybdenite), the complete dataset covers a total range in Mo isotope signatures from −1.6 to +1.8‰ δ^{98}Mo$_{SRM3134}$ with a bimodal distribution of heavy fluid and light minerals (Fig. 6), the largest range so far reported for an evolved igneous-hydrothermal system. The Mo isotopic composition of the initial, evolved bulk rocks varies over ca. 0.6‰, and overlaps with the isotopically heavy end of published Mo isotope data for igneous
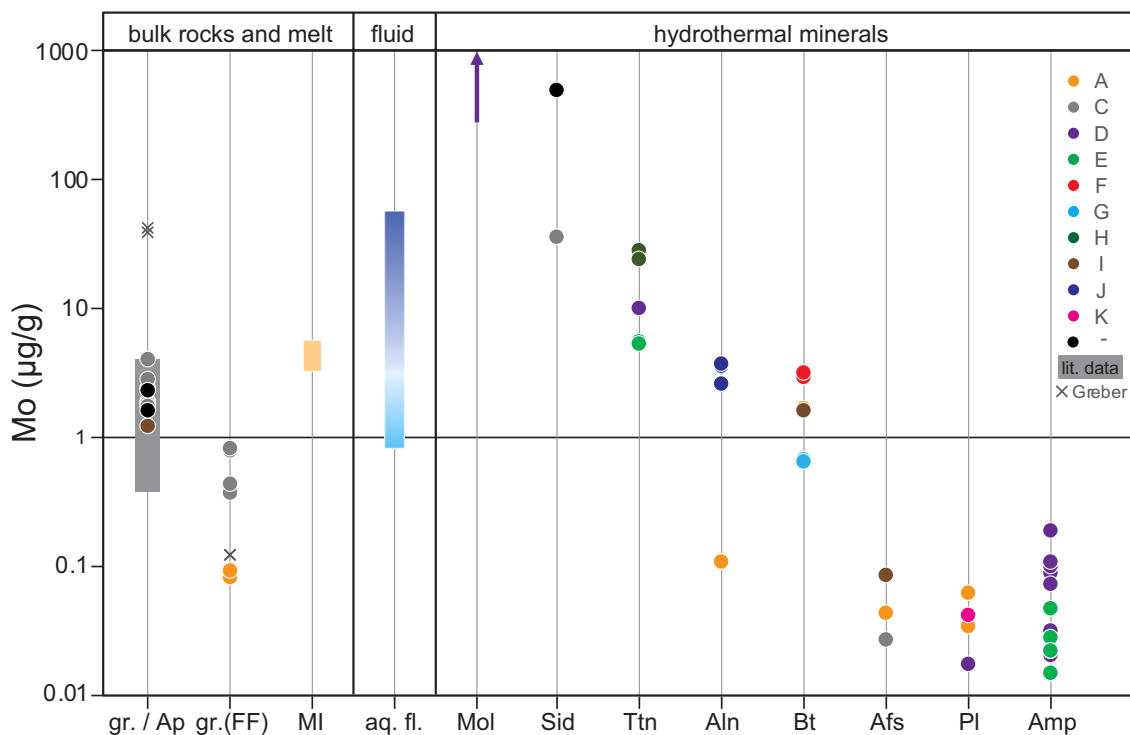
Fig. 7. Molybdenum concentrations of the phases investigated; gr./Ap includes regular granite samples and aplite sample Pa-34(Ap), gr.(FF) stands for granitic bulk rocks with fluid features, MI for melt inclusions, aq. fl. for aqueous hydrothermal fluid; mineral abbreviations after Whitney and Evans (2010). Bulk rock literature values displayed as dark grey band compiled for felsic rocks from Voegelin et al. (2014) and Yang et al. (2017), and as grey crosses for one granite and one rhyolite (due to fluid loss grouped with the FF samples) associated with the Mo-mineralised porphyry-type Questa deposit (NM, USA) from Greber et al. (2014). Melt (MI) and hydrothermal fluid (aq. fl.) concentration ranges determined from melt and fluid (vapour in light blue and brine in dark blue) inclusion assemblages in Torres del Paine miarolitic cavity quartz (Table A1.2). Hydrothermal minerals in order of overall decreasing Mo concentrations. Uncertainties for concentrations determined by ID MC-ICP-MS are estimated to 2% 2SD and thus smaller than symbol size. (For interpretation of the references to colour in this figure legend, the reader is referred to the web version of this article.)

rocks or arc lavas. Together, the very low $\delta^{98}Mo_{SRM3134}$ signatures of hydrothermal minerals and the heavy isotopic composition documented for the magmatic-hydrothermal fluid produce a primary isotopic variability of $>3‰$ $\delta^{98}Mo$ in magmatic-hydrothermal systems that exceeds the observed variation for most other sample types or settings (Fig. 6).

4.1. Distribution of Molybdenum in magmatic-hydrothermal phases

Molybdenum concentrations in the various phases present during the magmatic-hydrothermal evolution vary over almost four orders of magnitude, spanning a total range from <0.1 μg/g to several hundred μg/g (Fig. 7, Table 2), excluding molybdenite, which contains Mo as major constituent with ~60 wt%. Across several samples from this single locality, Mo concentrations can vary up to one order of magnitude for individual hydrothermal minerals, while bulk rock Mo concentrations display an even larger variation between 0.08 and 3.9 μg/g. These bulk rock concentration ranges overlap with published Mo concentration data for felsic rocks (e.g., Voegelin et al., 2014; Yang et al., 2017; Greaney et al., 2018), but tend to be more variable than so far determined for other settings.

Bulk rock Mo concentrations were obtained by both isotope dilution and LA-ICP-MS pressed powder pellet measurements (Table 2). Unless explicitly stated otherwise, Mo concentrations employed in this paper are ID data. Most of the data agree within measurement uncertainty between the two methods. Note that isotope dilution data are prominently higher for some samples, and Mo concentration data measured by LA-ICP-MS on pressed powder pellets display elevated uncertainties, thus indicating heterogeneity in Mo concentration (recall the observed molybdenite inclusions in magmatic quartz crystals; Fig. A2.4, and Audétat et al., 2011). To ensure direct comparability between Mo concentration data and isotopic compositions, Mo concentrations determined by isotope dilution will be used from here onwards as both were obtained from the same bulk rock powder digestion.

Molybdenum concentrations of granites generally fall into the range between 1.2 and 2.3 μg/g, the highest Mo concentration of 3.9 μg/g is observed for Bt-rich granite TdP15a(D). Thus, our bulk rock Mo concentrations overlap with the range so far reported for SiO_2-rich rocks (e. g., Hedenquist and Lowenstern, 1994; Candela and Blevin, 1995; Voegelin et al., 2014; Yang et al., 2017; Wille et al., 2018). Bulk rock samples with fluid features (see section 2.1) have comparatively lower Mo concentrations of 0.08–0.8 μg/g. Hence, they are depleted in Mo compared to granites without fluid features and published granite Mo concentrations, except for a post-mineralisation rhyolite dike with 0.12 μg/g Mo at the Questa Mo deposit (Greber et al., 2014; interpreted to reflect Mo loss due to earlier fluid exsolution).

Hydrothermal minerals display ranges in [Mo] between different and even within individual cavities that can amount to one order of magnitude (Fig. 7). Concentrations in Mo-bearing minerals range from 0.01 μg/g Mo in amphibole to 480 μg/g Mo in one siderite sample (Table 2), excluding virtually Mo-free quartz returning LA-ICP-MS LODs of ~0.003 μg/g Mo (for the largest beam size, see Table C.1).

In detail, Mo concentrations of several feldspar samples range from 0.02–0.06 μg/g in albite and from 0.03–0.08 μg/g in alkali feldspar (feldspar types identified based on LA-ICP-MS measurement, see Table C.1). We observe Mo concentration variability also between feldspars in different cavities, with higher [Mo] for feldspars in cavities A, I, and K, and lower values in C and D.

Biotite is also abundant in some cavities, and Mo concentrations for different Bt crystal samples range from 0.6 μg/g in cavity G, to 1.6 μg/g in cavities A and I to 2.9–3.1 μg/g in cavity F. Data indicate consistent Mo concentrations in a given cavity but significant variation between different cavities.

For the two sampled cavities in which amphibole is very abundant, repeated measurements of amphibole dry splits revealed a significant range in Mo concentration for cavity D (0.02–0.2 μg/g), but smaller variability and lower concentrations for cavity E (0.01–0.05 μg/g).

Molybdenum concentrations of individual mm to 1 cm sized allanite crystals from two cavities are highly variable. Cavity A allanite is very low in Mo, containing 0.1 μg/g only, while allanite crystals of cavity J have concentrations of 2.5–3.6 μg/g. Most rare earth element concentrations determined by LA-ICP-MS are also lower for cavity A allanite, but La concentrations of ca. 45′000 μg/g are similar for both cavities (Table C.1), confirming that measured crystals are allanite and not epidote.

Titanite represents a significant host for Mo, with concentrations ranging between 5 and 27 μg/g. Titanite crystals from cavity E and D cover the lower end of this range with concentrations of 5.2–5.4 μg/g and 9.8 μg/g, respectively, while cavity H titanite crystals have significantly higher concentrations ranging from 23.2 to 27.0 μg/g.

A few cavities with otherwise simple mineralogy (mainly cavity C) host siderite crystals overgrowing quartz and feldspar. They are significant carriers for Mo but apparently exhibit highly variable concentrations in and across samples. Our two samples possess 35 μg/g (28 ± 14 μg/g by LA-ICP-MS) and 480 μg/g Mo (260 ± 150 μg/g by LA-ICP-MS), respectively.

The documented differences in Mo concentrations between in situ LA-ICP-MS data and bulk dissolution MC-ICP-MS measurements for higher concentrated minerals (Ttn, Aln, Sid) indicates concentration variations for individual crystals of these minerals.

4.2. Molybdenum isotopic composition of magmatic and hydrothermal phases

Measured isotopic signatures of all magmatic-hydrothermal phases (bulk rock+melt, fluid, and hydrothermal minerals, see Table 2) are presented in Fig. 8, with distinctive colours and matching tie lines that illustrate bulk rock, fluid, and minerals coexisting in a given cavity. Two observations are immediately apparent, (i) the hydrothermal fluid is always heavier than the granitic host rocks and the minerals that crystallised from the fluid, and (ii) each phase displays variably prominent ranges in $\delta^{98}Mo$ between different cavities that are much larger than the ranges displayed by a given phase within a single cavity.

4.2.1. Bulk rock samples

The granitic bulk rock samples exhibit $\delta^{98}Mo_{SRM3134}$ ranging from -0.08 to $+0.26‰$. Transition zone samples from the vicinity of cavity C – TdP14(FF) and TdP21(FF) – fall into the middle of this range with values between $+0.04$ to $+0.10‰$, while sample Pa-05(FF) is characterised by slightly heavier isotopic compositions of $+0.26$ and $+0.31‰$ $\delta^{98}Mo_{SRM3134}$. The heaviest isotopic composition was observed for the late aplite Pa-34(Ap), with $\delta^{98}Mo_{SRM3134}$ of $+0.46‰$. The range in our bulk rock Mo isotopic compositions is slightly larger than, but overlaps with, those reported for evolved rocks in previous studies ($+0.05 < \delta^{98}Mo_{SRM3134} < +0.45$; e.g., Voegelin et al., 2014; Yang et al., 2017; Wille et al., 2018).

4.2.2. Mo isotopic signatures of magmatic fluid and silicate melt inclusions

$\delta^{98}Mo_{SRM3134}$ values of aqueous fluid inclusion-bearing quartz samples are between $+0.6$ to almost $+1.8‰$ ($n = 8$) and thus prominently heavier than the host granite from which the fluid exsolved (Fig. 8). Data for individually measured dry splits (cavity E: 1.55 and 1.73‰) agree well with each other within uncertainties. In order to test the sensitivity of bulk quartz dissolution data for the presence of melt inclusions in the hydrothermal quartz, quartz sample Pa-05 (cavity A) containing melt inclusions along with fluid inclusions was processed together with the other quartz samples, returning $+0.30‰$ $\delta^{98}Mo_{SRM3134}$, a signature that falls into the range of the bulk rock data with fluid features (Fig. 8).

4.2.3. Hydrothermal minerals

With a total range from -1.56 to $+0.56‰$ $\delta^{98}Mo_{SRM3134}$, the diverse hydrothermal minerals are consistently lighter than the magmatic fluid
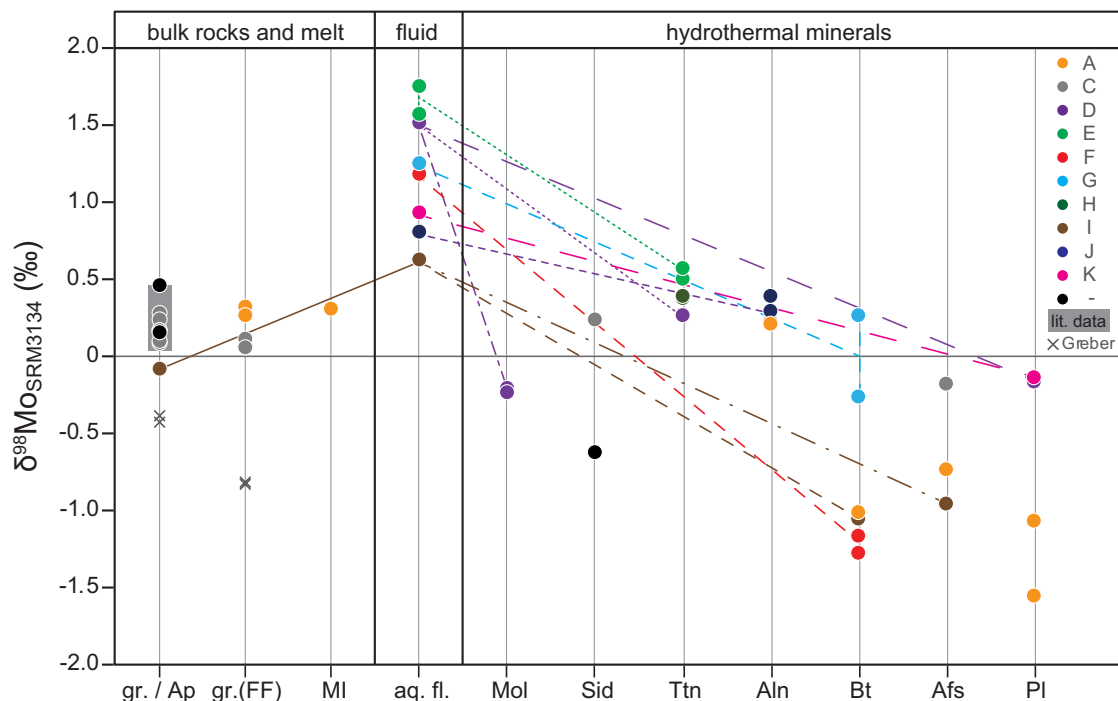
Fig. 8. Molybdenum isotopic signatures of the phases investigated; gr.(FF) stands for granitic bulk rocks with fluid features, MI for melt inclusions, aq. fl. for aqueous fluid, hydrothermal mineral abbreviations according to Whitney and Evans (2010), references for literature data as in Fig. 7. The colour-coded dashed lines connect fluid-mineral pairs in the same cavity. External reproducibility (2SD) of 0.08‰ (0.11‰ for low concentration samples) is smaller than the plotted symbols.

(Fig. 8). For individual minerals, several dry splits reveal slight variability in isotopic composition. However, as for Mo concentration data reported above, data for a given mineral vary significantly more between different cavities.

Molybdenum isotopic compositions of the most abundant minerals feldspar and biotite are typically light but highly variable between and even within some cavities. Values obtained for plagioclase range from

-1.56 to -0.14‰ $\delta^{98}Mo_{SRM3134}$ ($n = 4$), while alkali feldspar Mo signatures are slightly heavier with $\delta^{98}Mo_{SRM3134}$ between -0.96 and -0.19‰ ($n = 3$). The lowest values for both feldspars were observed for cavities A and I, while cavities C, D, and K constitute the highest end of the documented range. Biotite samples from cavities A, F, and I exhibit a very low $\delta^{98}Mo_{SRM3134}$ of between -1.28 and -1.01‰ ($n = 4$). In contrast, the low [Mo] biotite of cavity G, which is partly chloritised, is
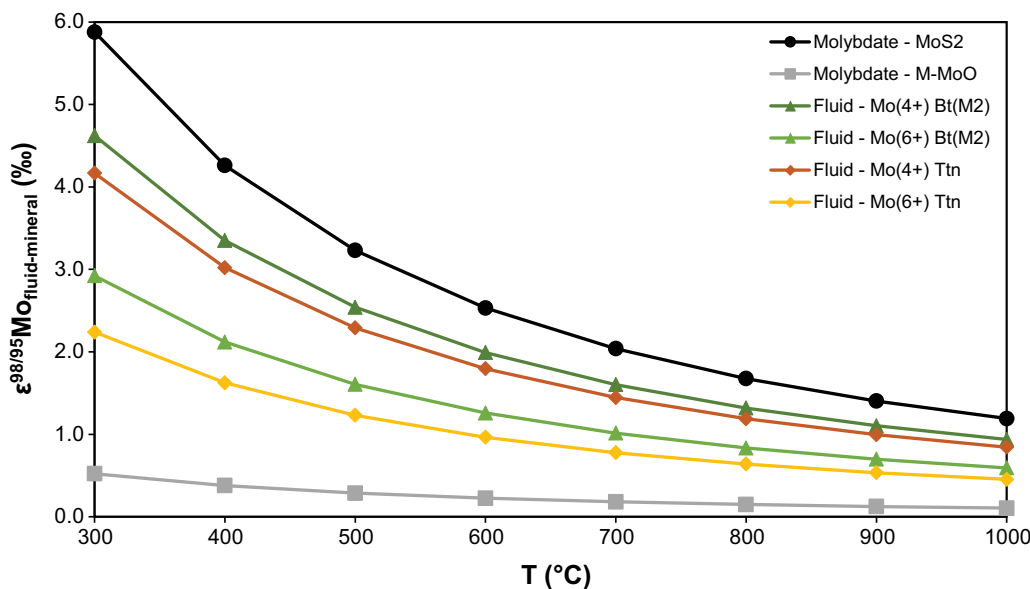
Fig. 9. Modelled isotopic fractionation $\varepsilon^{98}Mo_{fluid\text{-}mineral} = 1000\ \ln\alpha_{fluid\text{-}mineral}$ between oxidised molybdate (dominant Mo species in fluid and silicate melt) and different magmatic-hydrothermal phases including another Mo-oxide species (M-MoO; M = metal, e.g., Pb, Fe, Bi) chosen to approximate fluid-melt fractionation, molybdenite (MoS_2), biotite, and titanite as a function of temperature were calculated according to Young et al. (2015). The curves visualise the combined effects of changes in valence state, coordination and anion (O vs. S). For Ti-bearing silicate minerals biotite and titanite two scenarios were modelled, assuming Mo substitutes for Ti as either Mo^{6+} (light) or Mo^{4+} (dark).

distinctly heavier with values of −0.27 and +0.26‰ $\delta^{98}Mo_{SRM3134}$ ($n = 2$). No reliable Mo isotopic compositions could be obtained for the Fe-rich amphiboles, due to insufficient matrix separation during ion chromatographic purification procedures.

Minerals with higher Mo concentrations tend to possess heavier Mo isotopic compositions and be less variable. Titanite $\delta^{98}Mo_{SRM3134}$ ranges from +0.25 to +0.56‰ ($n = 5$), and allanite shows Mo isotopic signatures between +0.20 and +0.38‰ $\delta^{98}Mo_{SRM3134}$ ($n = 4$). Both these isotope signatures are lower than the fluid signature determined for the same cavity but largely overlap with the bulk granite range. Two siderite samples with [Mo] of 35 and 480 μg/g, respectively, have distinctly different isotopic signatures of +0.22‰ and −0.63‰ $\delta^{98}Mo_{SRM3134}$. Two dry splits of hydrothermal molybdenite found in cavity D have identical Mo isotopic compositions of −0.24 and −0.21‰ $\delta^{98}Mo_{SRM3134}$.

4.3. Modelled Mo isotope fractionation

Modelled fractionation factors were calculated according to Young et al. (2015) for various exchange reactions expected to occur during the magmatic-hydrothermal evolution of the miarolitic cavities, namely: molybdate – another Mo-oxide species (grey squares), molybdate – biotite (light and dark green triangles), molybdate – titanite (orange and yellow diamonds), and molybdate – molybdenite (black circles; all displayed in Fig. 9). All modelled curves exhibit the expected increase in equilibrium stable isotope fractionation with decreasing temperature. The relative differences between the modelled curves for the different species and potential forms of Mo incorporation in silicate minerals (Mo^{4+} or Mo^{6+}) visualise the effect of changes in valence state and coordination on Mo isotope fractionation.

The largest fractionation factors are obtained for the exchange between oxidised molybdate and reduced molybdenite (Fig. 9; black curve), while the smallest fractionation is observed between the two Mo-oxide species (grey curve in Fig. 9). The latter is taken to approximate Mo fractionation factors between fluid and melt that both contain oxidised Mo as molybdate (e.g. Farges et al., 2006; Rempel et al., 2009), as no structural data are available for the difference in the molybdate molecule in silicate melt vs. aqueous fluid. Resulting factors represent only maximum values for fluid-melt fractionation and are <0.2 over most of the temperature range. The values for biotite fall in the intermediate range. The two curves for biotite (Fig. 9, green curves) as well as titanite (Fig. 9, orange curves) reveal a stronger fractionation for the incorporation of reduced Mo^{4+} in silicates compared to the incorporation of oxidised Mo^{6+}. In both cases, fractionation is larger for biotite than for titanite. For feldspars and carbonates no information on either Mo or Ti incorporation in the crystal lattice could be identified. Therefore, we cannot derive the preferred occupation sites and associated structural parameters required to model Mo fractionation factors.

5. Discussion

In the following sections, we first characterise the processes that govern Mo distribution and isotope fractionation in evolving upper crustal magmatic-hydrothermal systems, as documented in the comprehensive dataset measured in this study, combined with results of theoretical calculations to devise a qualitative model for the complete magmatic-hydrothermal evolution of Mo in crystallising intrusions (section 5.1). Focussing on the hydrothermal evolution, we determine isotopic differences of coexisting fluid-mineral pairs to assess the extent of hydrothermal Mo isotope fractionation (section 5.2).

5.1. Mo distribution and isotope fractionation during magmatic-hydrothermal processes

The comprehensive dataset in this study attests to a large variability in Mo concentrations and isotopic compositions for the various phases, thus demonstrating that redistribution of Mo during magmatic and hydrothermal processes causes significant isotopic fractionation in a temperature range from ∼650 to ∼350 °C. The underlying processes documented by the bulk rock, fluid, and mineral data are addressed in the following paragraphs, starting out with a focus on late magmatic evolution and then concentrating on the hydrothermal stage.

5.1.1. Magmatic evolution and fluid exsolution

The granite bulk rock samples analysed in this study cover the highly evolved part of the igneous evolution of the TPIC at >72 wt% SiO_2. Measured $\delta^{98}Mo_{SRM3134}$ for granite bulk rocks showing no petrographic signs of fluid exsolution vary between −0.08 and +0.26‰. Continental arc magmas potentially experience crustal assimilation, which might introduce initial Mo isotopic variability long before the late stage magmatic processes investigated in this study. However, as such assimilation only played a limited role for the TPIC magmatic system (e. g. Leuthold et al., 2014; Müntener et al., 2018; Ewing et al., 2018), we assume that the system evolved from a uniform Mo isotope starting composition. In light of this, we interpret the significant variability observed in the highly evolved bulk rock samples as a sign that Mo isotope fractionation processes occurred during igneous evolution. Our bulk rock and melt inclusion (+0.3 $\delta^{98}Mo_{SRM3134}$) data agree well with the range in $\delta^{98}Mo_{SRM3134}$ (ca. +0.1 to +0.3‰) for fractionated arc rocks reported so far (Voegelin et al., 2014; Wille et al., 2018). The heaviest bulk rock Mo isotope composition of our data set (of +0.46‰ $\delta^{98}Mo_{SRM3134}$) was measured for aplitic granite sample Pa-34(Ap), which we interpret to indicate that the magma for this rock may be dominated by residual melt extracted from an already prominently crystallised granite magma by filter pressing, thus representing the most fractionated bulk rock sample of our data set that was not significantly affected by loss of heavy Mo into an exsolving fluid.

In comparison to granite plus aplite bulk rock data, the sample group of granites with fluid exsolution features reveals a variably prominent decrease in Mo concentration from 1.20–3.91 (average 2.16, $n = 7$) μg/g Mo in granites to 0.09–0.81 (average 0.51, $n = 4$) μg/g Mo in granites (FF), documenting variably prominent loss of Mo into an exsolving fluid phase. Any potential Mo isotopic fractionation associated with this process cannot be resolved by our sample data, as the documented Mo isotopic composition from −0.08 to +0.46‰ $\delta^{98}Mo_{SRM3134}$ in bulk rock samples without fluid features overlaps with the range from +0.04 to +0.31‰ $\delta^{98}Mo_{SRM3134}$ exhibited by the FF-samples. Our data thus suggest that there is no change in Mo speciation between hydrous melt and exsolving fluid at ca. 650 °C (see grey curve in Fig. 9) and that molybdate likely prevails (e.g., Farges et al., 2006; Rempel et al., 2009). Consequently, Mo isotopic fractionation could possibly occur only in response to differences in external coordination of the molybdate oxygens in polymerised melt or aqueous fluids, a possibility that cannot be tested by our data, however. We therefore conclude that Mo isotope fractionation may occur upon fluid exsolution from magma (as proposed by Greber et al., 2014, based on a light late granite dike that lost >99% of its Mo), but that its impact on the granite and fluid Mo reservoirs is very subordinate until the Mo fraction in one reservoir is very small.

5.1.2. Hydrothermal evolution

Recalling that a given miarolitic cavity represents a closed system from the timing of fluid exsolution onwards, Mo is continuously redistributed into crystallising hydrothermal minerals, depleting the fluid gradually in Mo with progressive hydrothermal evolution. Except for virtually Mo-free quartz ([Mo] below LOD of 0.003 μg/g), all investigated hydrothermal minerals contribute to the Mo mass balance in a given cavity. The Mo concentration dataset for all measured minerals reveals a tendency that highly abundant major silicate minerals (plagioclase, alkali feldspar, biotite, and amphibole) contain lower Mo concentrations, while concentrations are significantly higher for less abundant (titanite) or minor minerals (allanite, siderite, and of course molybdenite). Because the lower Mo concentration minerals are the most abundant ones in the cavities, each of them nevertheless

contributes significantly to the cavity Mo mass balance, notably biotite. Titanite crystals are typically either small and abundant, or rare but growing as large as 1 cm. Together with its medium to high (few to several tens of μg/g) Mo concentrations, titanite represents a major contributor to the cavity Mo mass balance. The largest direct effect on the cavity Mo mass balance is exerted by molybdenite crystallisation, if present. However, we only observed hydrothermally precipitated molybdenite in a single cavity (D). We do not attempt to quantify the cavity Mo isotope mass balance because the masses of each cavity phase (fluid and minerals) cannot be constrained.

The redistribution of Mo during the hydrothermal evolution encompasses Mo isotope fractionation between fluid and crystallising minerals in a given cavity, whereby the minerals are always preferentially enriched in light Mo isotopes relative to the coexisting fluid (Fig. 8). Accordingly, protracted mineral crystallisation (Fig. 5) in a closed system progressively removes Mo from the fluid into the crystallising minerals, where this Mo is locked away from further exchange with the cavity fluid. As a consequence, only the rim of a given mineral is in chemical and Mo isotopic equilibrium with the cavity-filling fluid at a given time. With the preferential removal of light Mo into minerals, the remaining hydrothermal fluid will evolve towards progressively higher δ^{98}Mo, which will directly be reflected in the Mo isotopic composition of crystallising minerals. This is true if bulk crystallisates preferentially incorporate Mo over water (structurally bound as OH in minerals), thus depleting the residual fluid in Mo, as is the case for dominant crystallisation of anhydrous minerals (e.g., quartz, feldspar, titanite) or for minerals with KD_{Mo}(fluid-mineral) >1, as observed in the cavities.

A first consequence of this process is that minerals which crystallise over a large interval of cavity evolution will incorporate successively heavier Mo isotopic compositions, accounting for the range in δ^{98}Mo measured for a given hydrothermal mineral in different cavities. Moreover, individual crystals should be zoned, with light Mo in the core and progressively heavier Mo towards the rim. Hence, we expect early precipitates to be lighter than later ones.

This is confirmed by the trend of increasingly heavier δ^{98}Mo with decreasing Mo concentration documented for a given mineral (Fig. 10). The consistent covariation of relative Mo concentrations (normalised to the average concentration for a given mineral) and corresponding changes in isotopic signatures for all hydrothermal mineral data (Fig. 10) attests to the cogenetic relationship of hydrothermal minerals in the closed system cavities. The effect is recorded most prominently by

minerals which continuously crystallised during the protracted cavity evolution such as feldspars and biotite, while the correlation is weak for higher concentrated minerals, e.g., titanite.

Our dataset thereby validates the concept above, as well as the previously postulated evolution of the fluid phase towards increasingly heavier Mo isotopic composition (e.g., Greber et al., 2014) with the first direct measurements of coexisting fluid and hydrothermal minerals.

A second consequence of the cogenetic hydrothermal evolution of fluid and minerals in a closed cavity system is that the hydrothermal fluid Mo isotope data should show the largest range of all cavity phases as the fluid is always present from the beginning to the end of cavity evolution. The smaller range of only <1.2‰ (+0.61 to +1.73‰ δ^{98}Mo$_{SRM3134}$) compared to a variability of up to 1.4 or 1.5‰ for biotite and plagioclase is interpreted to represent a direct consequence of the bulk quartz dissolution method. In this case, each fluid sample encompasses a priori unconstrained fractions of several fluid generations – as well as fluid phases vapour and brine – successively entrapped in the host quartz crystal. Owing to comparatively low fractions of fluid inclusions in quartz in general, the resolution of successive fluid generations based on single fluid inclusion assemblages was not possible, as at least 15–20 ng Mo were required for isotope ratio measurement. Our measured fluid inclusion Mo isotope compositions therefore represent averaged signatures, whereby the lowest measured Mo isotope signatures most closely approach the starting fluid signature – which was potentially even lower – while the highest measured Mo isotope signatures likely represent a marked underestimate of the latest, low Mo concentration fluid stages, which therefore are not well represented by the data. Consequently, the overall variability in measured fluid δ^{98}Mo$_{SRM3134}$ data only represents a minimum range for fluid Mo isotope signatures.

Bulk fluid Mo isotope data represent an unconstrained mixture of brine and vapour inclusions that coexisted during the magmatic-hydrothermal evolution of the cavities. Molybdenum speciation in brine and vapour may be different (e.g., Rempel et al., 2008, 2009; Ulrich and Mavrogenes, 2008; Borg et al., 2012), thus potentially fractionating the Mo isotopic ratios between the two coexisting phases. Because we cannot constrain the relative mass portions of brine and vapour in a given bulk fluid sample, our data do not allow us to assess the effect of possible brine - vapour Mo isotopic fractionation.

5.1.3. Conceptual model of Mo isotope fractionation in magmatic-hydrothermal systems

Based on the systematics of Mo distribution and isotope fractionation discussed above and taking into account previously published findings, we provide a conceptual model (Fig. 11) for the magmatic-hydrothermal evolution of a closed system cavity to illustrate the fundamental aspects of the Mo isotope evolution of the coexisting phases. This can serve as a framework for the subsequent assessment of Mo isotope fractionation under high to medium temperature hydrothermal conditions.

The magmatic evolution of granite is dominantly controlled by fractional crystallisation of mainly ±amphibole, ±magnetite, biotite, feldspar, and quartz. Upon crystallisation, these minerals preferentially incorporate light Mo isotopes (e.g., Voegelin et al., 2014; Wille et al., 2018), which results in an increasingly heavier Mo isotope composition of the residual melt during the magmatic evolution. Simultaneously, the continued crystallisation of these mostly anhydrous minerals eventually leads to fluid saturation of the residual melt and consequently the exsolution of a separate aqueous fluid. Bulk fluid – melt Mo partition coefficients of ~5–10 (e.g., Audétat and Pettke, 2003; Zajacz et al., 2008, and references therein), indicate preferential partitioning of Mo into the exsolving magmatic-hydrothermal fluid. Taking into account our data as well as findings from Greber et al. (2014), the Mo isotopic composition of this fluid might be slightly heavier than that of the coexisting residual melt. The more fluid exsolves, the more Mo is partitioned into the fluid phase, which eventually may lead to a Rayleigh distillation process in the last residual melt fractions that may go along
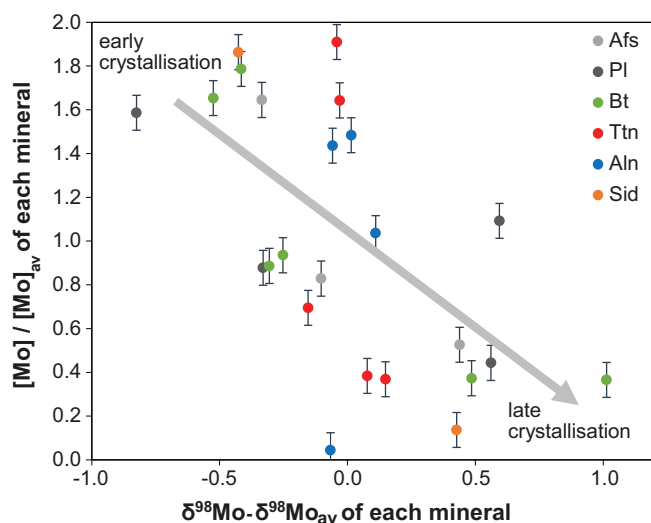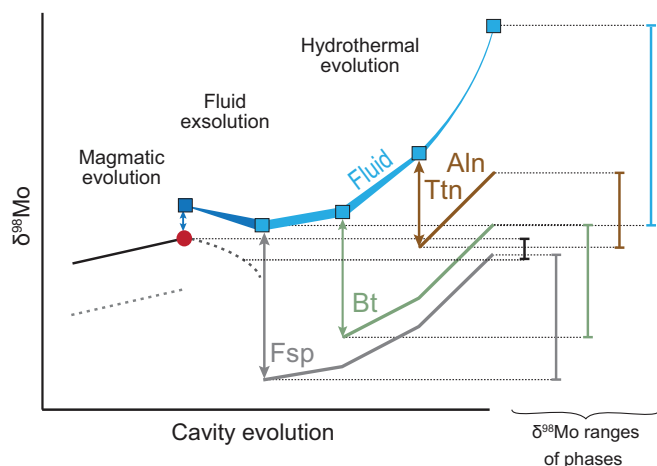

Fig. 10. Mo concentrations against isotopic compositions – individually normalised to the average for each mineral to exclude scatter introduced by variability in absolute values – reveal a consistent negative trend for most hydrothermal minerals with progressive hydrothermal evolution (grey arrow).

Fig. 11. Conceptual diagram illustrating our preferred interpretation of how δ^{98}Mo signatures of the various coexisting phases evolved, starting at the late magmatic stage and terminating when the cavity cooled to below ~300 °C (X-axis = cavity evolution). Vertical arrows illustrate the mineral-specific fluid-mineral Mo isotope fractionation, assumed to be constant (for simplicity) over the temperature range of mineral crystallisation. Ranges of measured δ^{98}Mo for each hydrothermal phase are displayed to the right. The magmatic evolution encompasses granitic magma crystallisation with Mo isotopic evolution shown for the sum of crystals (dashed line) coexisting with melt (solid black line) from which aqueous fluid starts to exsolve at the red point. We speculate (based on data in Greber et al., 2014) that the exsolving fluid (dark blue square) is slightly heavier than the melt (indicated by double-headed blue arrow). Progressive fluid exsolution (depicted by the first section of the blue band) evolves towards progressively lighter δ^{98}Mo (approximating the bulk rock signature) along with a progressively increasing mass of Mo hosted in the fluid. The residual melt (sketched with the black dashed line) becomes progressively depleted in Mo and evolves towards lighter δ^{98}Mo signatures. The first light blue square (beginning of the hydrothermal stage) represents the onset of hydrothermal mineral crystallisation (feldspar (Fsp) in light grey, followed by biotite (Bt) in light green, brown for allanite (Aln) and titanite (Ttn). The cumulative effect of hydrothermal mineral crystallisation drives the fluid δ^{98}Mo to progressively heavier values along with decreasing fluid Mo concentration (depicted by the thinning, light blue band between the squares), so that the last fluid stages may evolve via Rayleigh distillation (curved) to very heavy δ^{98}Mo. The measured, large ranges in δ^{98}Mo for a given phase thus record a specific duration of the overall magmatic-hydrothermal closed-system evolution. We propose that this conceptual evolution of Mo isotope ratios can be applied to all magmatic systems saturating a fluid phase in their crystallisation history, including those forming magmatic-hydrothermal ore deposits. (For interpretation of the references to colour in this figure legend, the reader is referred to the web version of this article.)

with a progressively lighter Mo isotope composition. The extremely light post-mineralisation rhyolite dike sample reported in Greber et al. (2014) was interpreted to represent such an example. In conclusion, the initial fluid Mo isotopic composition – representing the start of the hydrothermal evolution – should correspond to the melt from which it exsolves or may be slightly heavier as illustrated in Fig. 11.

During the subsequent hydrothermal evolution, the progressive precipitation of hydrothermal minerals preferentially removes light Mo isotopes from the magmatic-hydrothermal fluid. This in turn drives the remaining fluid to increasingly heavier isotopic compositions with time. In detail, we can sketch the hydrothermal evolution as follows (Fig. 11). For simplicity, it starts with crystallisation of feldspar only. Because feldspar Mo concentrations are very low (Table 2), this first step in the hydrothermal evolution will render the Mo isotope signature of the coexisting fluid only slightly heavier, controlled by the mass of crystallised feldspar. In a next step, biotite starts to crystallise, and the combined effect of feldspar and biotite crystallisation will deplete the fluid more significantly in Mo and drive the fluid Mo isotope composition towards distinctly heavier values. Minerals which start to crystallise

at a later stage during this evolution (here depicted by allanite and titanite) will tend to have heavier Mo isotope compositions when compared to early hydrothermal minerals. The crystallisation of minerals with higher Mo concentrations such as allanite and titanite – potentially on top of a continued crystallisation of feldspar and biotite – will then strongly deplete the fluid Mo, producing a Rayleigh distillation type evolution of the residual fluid with respect to its Mo isotope composition. In such a scenario, the isotopic signature of the most depleted, latest fluid generation can become very heavy. However, such very high fluid δ^{98}Mo cannot be confirmed by bulk quartz dissolution measurements, since these samples represent a mixture of successively entrapped fluid inclusion stages, the Mo isotope signature of which is likely dominated by early fluid increments with high Mo concentrations.

Because the hydrothermal minerals successively crystallise from an increasingly heavier hydrothermal fluid, they themselves will also span a considerable range in Mo isotope composition, even when assuming a constant fractionation factor between fluid and mineral during crystallisation. As protracted crystallisation of cavity minerals occurs during progressive cooling of the hydrothermal cavity system, the temperature-dependent increase in fractionation factors with decreasing T (Fig. 9) further enhances this effect. Finally, late-crystallised minerals are accordingly isotopically heavier than early ones, unless the increase in Mo isotope fractionation factor with decreasing temperature over-compensates for this trend.

5.2. Quantification of magmatic-hydrothermal Mo isotope fractionation

Because the hydrothermal cavity evolution is interpreted to have occurred under closed system equilibrium conditions, we can attempt to quantify Mo isotope fractionation factors based on our measurement data. As the measurement data of each sample represent an average over an increment of cavity evolution of a priori unknown duration, we chose a two-step approach. Based on the documented systematic evolution towards heavier isotopic compositions of all hydrothermal phases with progressive evolution (Figs. 10 and 11), we presume that the lightest isotopic composition measured for a given phase represents the earliest recorded signature, while the heaviest isotopic composition of that phase represents the latest documented increment. This allows us to calculate isotopic differences Δ^{98}Mo between earliest (Δ^{98}Mo$_1$(fluid-mineral)) and latest (Δ^{98}Mo$_2$(fluid-mineral)) increments of the fluid and each mineral (Fig. 12) from the combined dataset of all cavity samples:
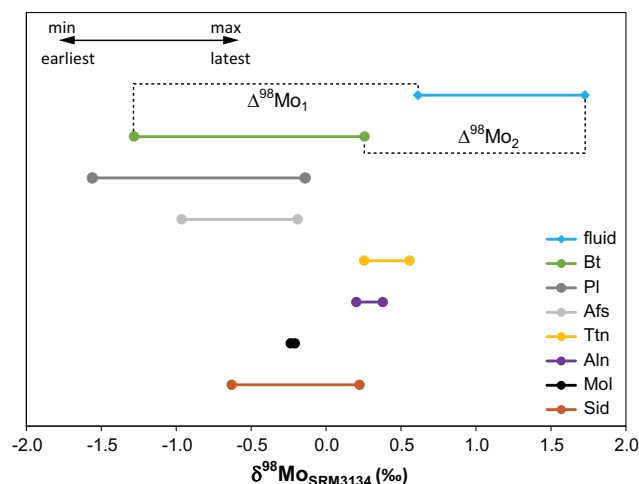
Fig. 12. Measured ranges in isotopic composition for all hydrothermal phases. The lower (higher) end of each range is assumed to represent the earliest (latest) recorded increment. As visualised by dashed lines, isotopic differences Δ^{98}Mo$_1$ and Δ^{98}Mo$_2$ for the fluid – biotite pair were calculated between the lowest and highest δ^{98}Mo pairs, respectively.

$$\Delta^{98}Mo_1(\text{fluid} - \text{mineral}) = \delta^{98}Mo_{\text{earliest fluid}} - \delta^{98}Mo_{\text{earliest mineral}} \quad (5)$$

$$\Delta^{98}Mo_2(\text{fluid} - \text{mineral}) = \delta^{98}Mo_{\text{latest fluid}} - \delta^{98}Mo_{\text{latest mineral}} \quad (6)$$

We obtain $\Delta^{98}Mo_{\text{fluid-plagioclase}}$ of between 1.9 and 2.2‰, $\Delta^{98}Mo_{\text{fluid-alkali feldspar}}$ of between 1.6 and 1.9‰, and $\Delta^{98}Mo_{\text{fluid-biotite}}$ of between 1.5 and 1.9‰. This demonstrates strong Mo isotopic fractionation already during the early, high temperature stage (ca. 500–650 °C) of the hydrothermal evolution for these volumetrically abundant minerals with low (Afs, Pl) to intermediate (Bt) Mo concentrations. For minerals with higher Mo concentrations that are less abundant and likely crystallised across a smaller interval during later stages of cavity evolution, the extent of Mo isotope fractionation tends to be smaller, with measured $\Delta^{98}Mo_{\text{fluid-titanite}}$ ranging from 0.4 to 1.2‰, $\Delta^{98}Mo_{\text{fluid-allanite}}$ from 0.4 to 1.3‰, $\Delta^{98}Mo_{\text{fluid-molybdenite}}$ from 0.8 to 1.9‰, and $\Delta^{98}Mo_{\text{fluid-siderite}}$ from 1.2 to 1.5‰. We explain the larger difference between $\Delta^{98}Mo_1$ and $\Delta^{98}Mo_2$ for these minerals (except for siderite) to result from the fact that the complete range in fluid signatures is combined with signatures of minerals that most likely crystallised only late during cavity evolution across a short interval. Assuming late crystallisation for these minerals, $\Delta^{98}Mo_2$ should be more representative of the true fractionation effect, and might still only be a minimum estimate in case the coexisting late fluid was isotopically heavier than documented by our samples.

Because the hydrothermal phases evolved together under closed system equilibrium conditions these two calculated values bracket the range in isotopic differences that must include the true value corresponding to equilibrium conditions for the given fluid-mineral pair. In this case, the measured difference in Mo isotope composition between two phases is equal to the isotopic fractionation ε and can be related to the isotopic fractionation factor α as follows:

$$\Delta^{98}Mo_{\text{fluid}-\text{mineral}} (\text{measured}) = \varepsilon_{\text{fluid}-\text{mineral}} [‰] = 1000 \ln \alpha_{\text{fluid}-\text{mineral}} \quad (7)$$

Using the documented range in isotopic differences $\Delta^{98}Mo_1$ and $\Delta^{98}Mo_2$, we can thus constrain a range for the equilibrium fractionation factor α controlling the Mo exchange reaction for a fluid-mineral pair. The obtained ranges for each fluid – hydrothermal mineral pair are reported in Table 3.

Uncertainties associated with the range in isotopic differences obtained by this approach from the complete dataset of multiple cavities may include (i) slight temperature differences during mineral crystallisation in different cavities and correspondingly larger or smaller fractionation factors as a function of temperature, or (ii) different crystallising mineral assemblages that might exert a stronger or weaker fractionation effect on the fluid phase and in turn the mineral precipitates in an individual cavity.

Table 3
Mo isotopic differences ($\Delta^{98}Mo_{\text{fluid-mineral}}$) calculated from minimum and maximum measured signatures of magmatic-hydrothermal fluid and hydrothermal minerals and range for Mo isotope fractionation factors (α) between fluid and mineral in equilibrium derived from the ranges in $\Delta^{98}Mo$.

Mineral	$\Delta^{98}Mo_1$ (‰)	$\Delta^{98}Mo_2$ (‰)	Range for α*	Stage/Conditions
Plagioclase	2.2	1.9	1.0019–1.0022	Early/high T
Biotite	1.9	1.5	1.0015–1.0019	Early/high T
Alkali feldspar	1.6	1.9	1.0016–1.0019	Early/high T
Siderite	1.2	1.5	1.0012–1.0015	Later/lower T
Molybdenite	0.8	1.9	1.0008–1.0019	Timing unconstrained
Titanite	0.4	1.2	1.0004–1.0012	Intermediate
Allanite	0.4	1.3	1.0004–1.0013	Intermediate

* assuming that fluid and mineral pairs coexisted in equilibrium.

5.2.1. Measured $\Delta^{98}Mo_{\text{fluid-mineral}}$ in the context of modelled fractionation and literature data

For this study, modelled fractionation factors were calculated assuming that the dominant species in aqueous fluids in pH neutral rock-buffered magmatic-hydrothermal systems is oxidised molybdate, as observed experimentally at lower temperatures (e.g. Rempel et al., 2009; Borg et al., 2012). Both the absence of a resolvable fractionation effect during fluid exsolution (see section 5.1.1) from hydrous silicate melt containing Mo in the form of molybdate (e.g., Farges et al., 2006), and the absence of a correlation between Mo fluid-melt partition coefficients and Cl (e.g. Zajacz et al., 2008; Iveson et al., 2019) support the assumption that alternative species only play a minor role in these settings also at higher temperatures.

Our measured mineral concentration data suggest that Mo in hydrothermal systems preferably accumulates in Fe- and Ti-bearing silicates such as titanite and biotite, in analogy to magmatic systems (e.g., Voegelin et al., 2014; Yang et al., 2017; Greaney et al., 2018). This indicates that Mo distribution in hydrothermal environments is also governed by substitution of Mo for Ti based on the similar ionic radii (Shannon, 1976; Zack et al., 2002), justifying the assumptions made to
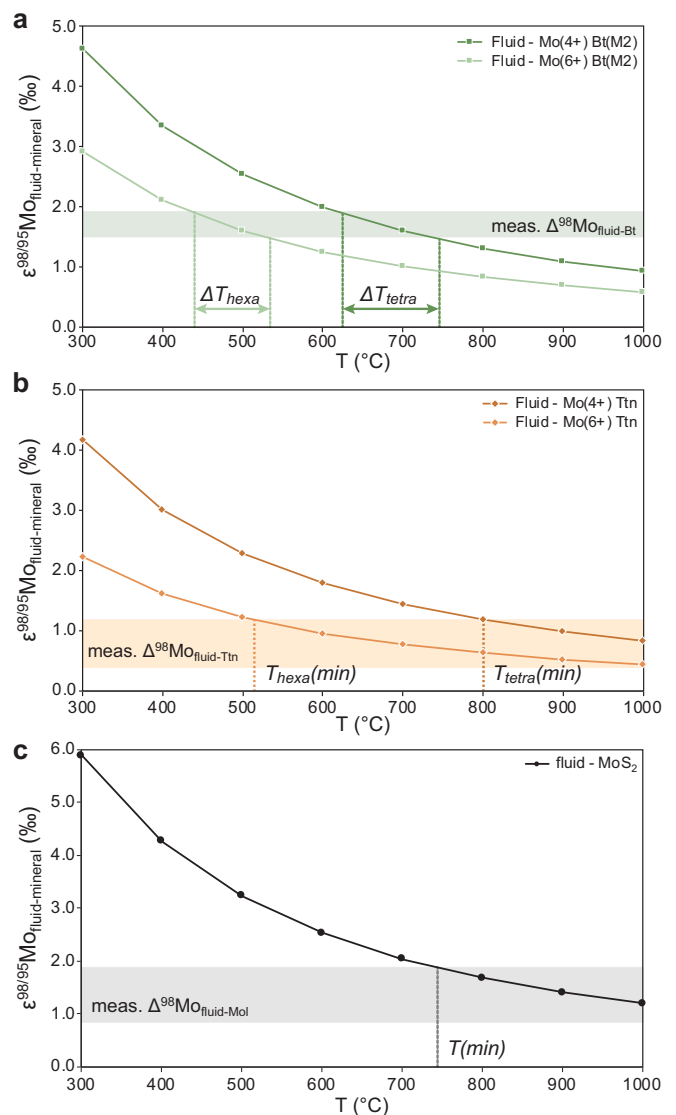
Fig. 13. Comparison of calculated isotopic differences $\Delta^{98}Mo$ from measured $\delta^{98}Mo$ of fluid-mineral pairs with theoretical Mo isotope fractionation ε (see section 4.3) constrains crystallisation temperatures and preferred Mo valence state for a: biotite; b: titanite, c: molybdenite.

model Mo isotope fractionation factors in section 4.3.

Fig. 13a compares the measured range in $\Delta^{98}Mo_{fluid-biotite}$ with the theoretical fractionation modelled for tetravalent and hexavalent Mo as a function of temperature. The documented isotopic difference can be explained by fractionation associated with the incorporation of oxidised Mo^{6+} in biotite between ~430 to ~530 °C. This is in good agreement with realistic formation temperatures of biotite in the miarolitic cavities that mostly overgrew early crystallised hydrothermal quartz and feldspar. In contrast, the temperature range of ~630 to ~750 °C for tetravalent Mo partly exceeds the 650–700 °C estimated for aqueous fluid exsolution from magma. Similarly, Fig. 13b suggests that Mo^{6+} is also the prevailing oxidation state incorporated in crystallising titanite (in agreement with crystallisation temperatures of ~520 °C), while Mo^{4+} incorporation would suggest minimum titanite crystallisation temperatures exceeding 800 °C that are well above granite liquidus conditions. For both Mo valence states, the lower end of the $\Delta^{98}Mo_{fluid-titanite}$ range (corresponding to $\Delta^{98}Mo_1$) would only be expected at significantly higher temperatures that are unreasonable for felsic, hydrous systems and hydrothermal conditions. This further supports that $\Delta^{98}Mo_2$ more closely reflects the true isotopic fractionation, confirming that titanite most likely precipitated from a later, isotopically heavy fluid.

Following these considerations, our data consolidate that Mo incorporation in hydrothermal silicates takes place in the form of Mo^{6+} (e.g., Willbold and Elliott, 2017, and references therein), indicating that changes in Mo valence state between coexisting phases (here fluid and minerals) are not required to account for the observed Mo isotope fractionation, as has been hypothesised previously (e.g., Greber et al., 2014; Voegelin et al., 2014). Rather, differences in bonding environment of Mo^{6+} in minerals compared to fluid may be the dominant parameter for isotope fractionation during hydrothermal processes. The good agreement between measured isotopic differences and modelled fluid - mineral fractionation factors for hexavalent Mo strongly supports the assumption that structural information for Ti incorporation in hydrothermal minerals is also applicable to Mo, as well as that molybdate was the prevailing Mo species in the magma-derived cavity fluid.

We can further compare the documented isotopic differences and theoretical fractionation data for fluid and molybdenite, which solely incorporates reduced Mo^{4+} and for which direct structural data are available (Bart and Ragaini, 1980). The minimum temperature of ~750 °C which would correspond to the maximum measured isotopic difference of 1.9‰ (Fig. 13c) is ca. 50–100 °C higher than the fluid exsolution temperature, and likely another 200 °C higher than reasonable crystallisation temperatures for hydrothermal molybdenite during subsequent cavity evolution. Most likely, this discrepancy arises from (i) near-quantitative removal of Mo from the fluid into crystallising molybdenite. In this case, the molybdenite isotopic signature would only exhibit a weak effect of isotopic fractionation; and (ii) the fact that our fluid samples do not represent the fluid from which molybdenite was precipitated. A fluid undergoing molybdenite crystallisation will be severely depleted in Mo and strongly fractionated. However, due to its low Mo concentration it will not contribute significantly to the fluid signature obtained by the bulk quartz dissolution method. The measured fluid samples obtained by bulk quartz dissolution are likely to represent pre molybdenite crystallisation fluid fractions with high Mo concentration and lighter isotopic composition. Therefore, the calculated $\Delta^{98}Mo_{fluid-molybdenite}$ represents a minimum value only (Figs. 12, 13), and larger $\Delta^{98}Mo$ values would be consistent with molybdenite crystallisation at lower T).

Finally, we could not model the expected isotope fractionation associated with Mo incorporation into feldspar due to a lack of information on how Mo is incorporated into its structure. We only note that the large isotopic differences evident from our measurement data indicate large Mo isotopic fractionation factors which could be caused by weaker bonding of Mo in the feldspar structures or possibly incorporation of more reduced Mo or a combination thereof.

For systems in which the preferred speciation of Mo in aqueous fluid

and silicate melts is molybdate (Farges et al., 2006; Rempel et al., 2009), we hypothesise that the ranges in fluid-mineral fractionation factors determined in this study may be applicable to estimate mineral-melt fractionation in comparatively oxidised magmatic systems, of course taking into account the differences in temperatures between hydrothermal and magmatic settings.

6. Conclusions and implications

This study provides the first comprehensive Mo isotope dataset for samples recording the entire magmatic-hydrothermal evolution from the point of fluid exsolution from magma at ~650 °C down to ca. 300 °C. The miarolitic cavity samples from the Torres del Paine intrusive complex represent closed system equilibrium evolution and document a very large total range in measured $\delta^{98}Mo_{SRM\ 3134}$ from −1.6 to +1.8‰. The measured large ranges in Mo concentrations and isotopic signatures demonstrate that magmatic-hydrothermal processes can exert a fundamental control on the distribution and isotopic composition of Mo in evolved igneous systems in the upper crust. This indicates that Mo isotopes in evolved magmatic rocks as well as hydrothermal fluids and associated minerals are highly sensitive to redistribution and fractionation processes.

Our findings offer insight into the mechanism that can produce the prominent variability and large ranges in Mo isotope ratios reported for hydrothermal molybdenite ore deposits (most recently e.g., Chang et al., 2020, and references therein). Hence, Mo isotope compositions of molybdenites are not well suited for metal source tracing of hydrothermal systems or ore deposits unless the effects of the prominent fractionation processes could be reliably corrected for. Our considerations do not negate that source-related isotopic variations can and likely do occur in igneous and hydrothermal systems. However, such initial variation is likely to be overprinted by subsequent redistribution and fractionation processes.

The key findings of this study improve our understanding of magmatic and hydrothermal Mo isotope fractionation processes at elevated temperatures and are summarised here:

a) Measured fluid signatures show that magmatic-hydrothermal fluids possess heavier $\delta^{98}Mo_{SRM\ 3134}$ than the magmas from which they originate.

b) Hydrothermal minerals exhibit highly variable isotopic signatures but are consistently lighter than the fluid from which they crystallised. Successive precipitation of hydrothermal minerals scavenges light Mo from the source fluid and thus results in increasingly heavier fluid Mo with progressive evolution of the hydrothermal system. Late hydrothermal minerals therefore tend to be heavier than early ones.

c) Our data provide large isotopic differences $\Delta^{98}Mo_{fluid-mineral} = \delta^{98}Mo_{fluid} - \delta^{98}Mo_{mineral}$ of up to 2.2‰ at temperatures of between ~650 and ~350 °C. In detail, we determined $\Delta^{98}Mo_{fluid-plagioclase}$ of 1.9–2.2‰, $\Delta^{98}Mo_{fluid-alkali\ feldspar}$ of 1.6–1.9‰, $\Delta^{98}Mo_{fluid-biotite}$ of 1.5–1.9‰; $\Delta^{98}Mo_{fluid-siderite}$ of 1.2–1.5‰, $\Delta^{98}Mo_{fluid-titanite}$ of (0.4 –) 1.2‰, $\Delta^{98}Mo_{fluid-allanite}$ of (0.4 –) 1.3‰, and $\Delta^{98}Mo_{fluid-molybdenite}$ of 0.8–1.9‰.

d) Given that equilibrium conditions prevailed during hydrothermal mineral crystallisation, our measured $\Delta^{98}Mo_{fluid-mineral}$ ranges constrain the Mo isotope fractionation factors α for the given fluid-mineral pairs.

e) Direction and magnitude of measured Mo isotopic fractionation agree with theoretical $\varepsilon^{98}Mo_{A-B} = 1000\ ln\alpha_{A-B}$ for incorporation as oxidised Mo^{6+} in hydrothermal minerals (except for molybdenite that incorporates Mo^{4+}), thus documenting that significant fractionation can occur without changes in Mo valence. Stronger fractionation is indicated for low Mo concentration phases in comparison to Mo-rich phases in accordance with principles of Rayleigh fractionation. Our model predicts larger isotope fractionation factors between fluid and molybdenite than for silicate minerals at a given

temperature reflecting the fact that molybdenite incorporates reduced, tetravalent Mo in its sulphide structure.

Because isotope fractionation factors represent an intensive property of a system at equilibrium, our measurement data can be taken as representative for any hydrothermal system undergoing crystallisation at elevated temperatures. Consequently, the very large extent of magmatic-hydrothermal Mo isotope fractionation documented here strongly suggests that initial Mo isotope variability likely becomes obliterated by fractionation processes during magmatic-hydrothermal evolution.

The prominent magmatic-hydrothermal Mo isotope fractionation and redistribution paired with incongruent weathering processes are likely causes for a variable continental Mo isotope runoff, possibly much more variable than so far acknowledged in models on the global Mo isotope cycle.

Contributions

AKCK: Sampling, sample selection and characterisation (including Raman spectroscopy and mineral LA-ICP-MS), sample preparation for MC-ICP-MS Mo isotope measurements, data reduction and interpretation, drafting of manuscript and critical revision.

TP: Sampling and sample selection, assistance with LA-ICP-MS, discussion of data and interpretation, editing of manuscript and critical revision.

MW: Guidance with sample dissolution and ion chromatography, assistance with MC-ICP-MS measurements, data reduction, discussion of data and interpretation, critical revision.

Declaration of Competing Interest

The authors declare that they have no known competing financial interests or personal relationships that could have appeared to influence the work reported in this paper.

Acknowledgements

Appendix A. Supplementary data

Supplementary data to this article can be found online at https://doi.org/10.1016/j.chemgeo.2021.120319.

References

Anbar, A.D., 2004. Molybdenum stable isotopes: observations, interpretations and directions. Rev. Mineral. Geochem. 55, 429–454.

Anbar, A.D., Duan, Y., Lyons, T.W., Arnold, G.L., Kendall, B., Creaser, R.A., Kaufman, A. J., Gordon, G.W., Scott, C., Garvin, J., Buick, R., 2007. A whiff of oxygen before the great oxidation event? Science 317, 1903–1906. https://doi.org/10.1126/science.1140325.

Archer, C., Vance, D., 2008. The isotopic signature of the global riverine molybdenum flux and anoxia in the ancient oceans. Nat. Geosci. 1 (9), 597–600. https://doi.org/10.1038/ngeo282.

Arnold, G.L., Anbar, A.D., Barling, J., Lyons, T.W., 2004. Molybdenum isotope evidence for widespread anoxia in mid-proterozoic oceans. Science 304, 87–90. https://doi.org/10.1126/science.1091785.

Audétat, A., Pettke, T., 2003. The magmatic-hydrothermal evolution of two barren granites: a melt and fluid inclusion study of the Rito del Medio and Canada Pinabete plutons in northern New Mexico (USA). Geochim. Cosmochim. Acta 67 (1), 97–121.

Audétat, A., Pettke, T., Heinrich, C.A., Bodnar, R.J., 2008. The composition of magmatic-hydrothermal fluids in barren and mineralized intrusions. Econ. Geol. 103, 877–908.

Audétat, A., Dolejš, D., Lowenstern, J.B., 2011. Molybdenite saturation in silicic magmas: Occurrence and petrological implications. J. Petrol. 52 (5), 891–904. https://doi.org/10.1093/petrology/egr008.

Barling, J., Arnold, G.L., Anbar, A.D., 2001. Natural mass-dependent variations in the isotopic composition of molybdenum. Earth Planet. Sci. Lett. 193, 447–457.

Bart, J.C.J., Ragaini, V., 1980. Molybdenum-Sulphur Bond-Strength Bond-Length Relationships. Phosphorus and Sulfur and the Related Elements 8 (2), 161–169. https://doi.org/10.1080/03086648008078182.

Baumgartner, L.P., Putlitz, B., Bodner, R., Leuthold, J., Müntener, O., Michel, J., 2012. Field guide to the Torres del Paine Igneous Complex and its contact aureole, pp. 1–39.

Bezard, R., Fischer-Gödde, M., Hamelin, C., Brennecka, G.A., Kleine, T., 2016. The effects of magmatic processes and crustal recycling on the molybdenum stable isotopic composition of Mid-Ocean Ridge Basalts. Earth Planet. Sci. Lett. 453, 171–181. https://doi.org/10.1016/j.epsl.2016.07.056.

Borg, S., Liu, W., Etschmann, B., Tian, Y., Brugger, J., 2012. An XAS study of molybdenum speciation in hydrothermal chloride solutions from 25-385°C and 600 bar. Geochim. Cosmochim. Acta 92, 292–307. https://doi.org/10.1016/j.gca.2012.06.001.

Breillat, N., Guerrot, C., Marcoux, E., Négrel, P., 2016. A new global database of δ98Mo in molybdenites: a literature review and new data. J. Geochem. Explor. 161, 1–15. https://doi.org/10.1016/j.gexplo.2015.07.019.

Burkhardt, C., Hin, R.C., Kleine, T., Bourdon, B., 2014. Evidence for Mo isotope fractionation in the solar nebula and during planetary differentiation. Earth Planet. Sci. Lett. 391, 201–211. https://doi.org/10.1016/j.epsl.2014.01.037.

Candela, P.A., 1997. A review of shallow, ore-related granites: Textures, volatiles, and ore metals. J. Petrol. 38, 1619–1633. https://doi.org/10.1093/petroj/38.12.1619.

Candela, P.A., Blevin, P.L., 1995. Do some miarolitic granites preserve evidence of magmatic volatile phase permeability? Econ. Geol. 90 (8), 2310–2316.

Candela, P.A., Holland, H.D., 1984. The partitioning of copper and molybdenum between silicate melts and aqueous fluids. Geochim. Cosmochim. Acta 48, 373–380. https://doi.org/10.1016/0016-7037(84)90257-6.

Casalini, M., Avanzinelli, R., Tommasini, S., Elliott, T., Conticelli, S., 2019. Ce/Mo and molybdenum isotope systematics in subduction-related orogenic potassic magmas of Central-Southern Italy. Geochem. Geophys. Geosyst. 20, 2753–2768. https://doi.org/10.1029/2019gc008193.

Chang, J., Li, J.W., Zhou, L., 2020. Molybdenum isotopic fractionation in the Tibetan Yulong Cu-Mo deposit and its implications for mechanisms of molybdenite precipitation in porphyry ore systems. Ore Geol. Rev. 123, 103571. https://doi.org/10.1016/j.oregeorev.2020.103571.

Chen, S., Hin, R.C., John, T., Brooker, R., Bryan, B., Niu, Y., Elliott, T., 2019. Molybdenum systematics of subducted crust record reactive fluid flow from underlying slab serpentine dehydration. Nat. Commun. 10 (1), 4773. https://doi.org/10.1038/s41467-019-12696-3.

Chukanov, N.V., Rozenberg, K.A., Rastsvetaeva, R.K., Möckel, S., 2008. New data on titanium-rich biotite: a problem of "Wodanite.". New Data on Minerals 43, 72–77.

Coplen, T.B., 2011. Guidelines and recommended terms for expression of stable-isotope-ratio and gas-ratio measurement results. Rapid Commun. Mass Spectrom. 25 (17), 2538–2560. https://doi.org/10.1002/rcm.5129.

Dickson, A.J., 2017. A molybdenum-isotope perspective on Phanerozoic deoxygenation events. Nat. Geosci. 10 (10), 721–726. https://doi.org/10.1038/ngeo3028.

Driesner, T., Heinrich, C.A., 2007. The system H2O-NaCl. Part I: Correlation formulae for phase relations in temperature-pressure-composition space from 0 to 1000 °C, 0 to 5000 bar, and 0 to 1 X-NaCl. Geochim. Cosmochim. Acta 71 (20), 4880–4901. https://doi.org/10.1016/j.gca.2006.01.033.

Ewing, T.A., Müntener, O., Leuthold, J., Ramirez de Arellano, C., Baumgartner, L.P., Schaltegger, U., 2018. The zircon Hf isotope archive of rapidly changing mantle sources in the south Patagonian retro-arc. Bull. Geol. Soc. Am. 131 (3–4), 587–608. https://doi.org/10.1130/B31983.1.

Farges, F., Siewert, R., Ponader, C.W., Brown, G.E., Pichavant, M., Behrens, H., 2006. Structural environments around molybdenum in silicate glasses and melts. II. Effect of temperature, pressure, H2O, halogens and sulfur. Can. Mineral. 44 (3), 755–773. https://doi.org/10.2113/gscanmin.44.3.755.

Freymuth, H., Vils, F., Willbold, M., Taylor, R.N., Elliott, T., 2015. Molybdenum mobility and isotopic fractionation during subduction at the Mariana arc. Earth Planet. Sci. Lett. 432, 176–186. https://doi.org/10.1016/j.epsl.2015.10.006.

Freymuth, H., Elliott, T., van Soest, M., Skora, S., 2016. Tracing subducted black shales in the Lesser Antilles arc using molybdenum isotope ratios. Geology 44, 987–990. https://doi.org/10.1130/G38344.1.

Gaschnig, R.M., Reinhard, C.T., Planavsky, N.J., Wang, X., Asael, D., Chauvel, C., 2017. The molybdenum isotope system as a tracer of slab input in subduction zones: an

example from Martinique, Lesser Antilles Arc. Geochem. Geophys. Geosyst. 18 (12), 4674–4689. https://doi.org/10.1002/2017gc007085.

Goldberg, T., Gordon, G., Izon, G., Archer, C., Pearce, C.R., McManus, J., Anbar, A.D., Rehkämper, M., 2013. Resolution of inter-laboratory discrepancies in Mo isotope data: an intercalibration. J. Anal. At. Spectrom. 28 (5), 724–735. https://doi.org/10.1039/c3ja30375f.

Greaney, A.T., Rudnick, R.L., Gaschnig, R.M., Whalen, J.B., Luais, B., Clemens, J.D., 2018. Geochemistry of molybdenum in the continental crust. Geochim. Cosmochim. Acta 238, 36–54. https://doi.org/10.1016/j.gca.2018.06.039.

Greber, N.D., Hofmann, B.A., Voegelin, A.R., Villa, I.M., Nägler, T.F., 2011. Mo isotope composition in Mo-rich high- and low-T hydrothermal systems from the Swiss Alps. Geochim. Cosmochim. Acta 75 (21), 6600–6609. https://doi.org/10.1016/j.gca.2011.08.034.

Greber, N.D., Siebert, C., Nägler, T.F., Pettke, T., 2012. $\delta^{98/95}$Mo values and molybdenum concentration data for NIST SRM 610, 612 and 3134: Towards a common protocol for reporting Mo data. Geostand. Geoanal. Res. 36 (3), 291–300. https://doi.org/10.1111/j.1751-908X.2012.00160.x10.1111/j.1751-908X.2014.12047.x.

Greber, N.D., Pettke, T., Nägler, T.F., 2014. Magmatic–hydrothermal molybdenum isotope fractionation and its relevance to the igneous crustal signature. Lithos 190–191, 104–110. https://doi.org/10.1016/j.lithos.2013.11.006.

Guillong, M., Meier, D.L., Allan, M.M., Heinrich, C.A., Yardley, B.W.D., 2008. Appendix A6: SILLS: a MATLAB-based program for the reduction of Laser-Ablation ICP–MS data of homogeneous materials and inclusions. In: Sylvester, P. (Ed.): Laser ablation ICP-MS in the Earth sciences: current practices and outstanding issues. Mineralogical Association of Canada Short Course Series 40, 328–333.

Hannah, J.L., Stein, H.J., Wieser, M.E., de Laeter, J.R., Varner, M.D., 2007. Molybdenum isotope variations in molybdenite: Vapor transport and Rayleigh fractionation of Mo. Geology 35 (8), 703–706. https://doi.org/10.1130/G23538A.1.

Hawthorne, F.C., Oberti, R., 2007. Amphiboles: Crystal chemistry. Rev. Mineral. Geochem. 67, 1–54. https://doi.org/10.2138/rmg.2007.67.1.

Hedenquist, J.W., Lowenstern, J.B., 1994. The role of magmas in the formation of hydrothermal ore-deposits. Nature 370, 519–527. https://doi.org/10.1038/370519a0.

Hin, R.C., Burkhardt, C., Schmidt, M.W., Bourdon, B., Kleine, T., 2013. Experimental evidence for Mo isotope fractionation between metal and silicate liquids. Earth Planet. Sci. Lett. 379, 38–48. https://doi.org/10.1016/j.epsl.2013.08.003.

Hin, R.C., Burnham, A.D., Gianolio, D., Walter, M.J., Elliott, T., 2019. Molybdenum isotope fractionation between Mo^{4+} and Mo^{6+} in silicate liquid and metallic Mo. Chem. Geol. 504, 177–189. https://doi.org/10.1016/j.chemgeo.2018.11.014.

Holzheid, A., Borisov, A., Palme, H., 1994. The effect of oxygen fugacity and temperature on solubilities of nickel, cobalt, and molybdenum in silicate melts. Geochim. Cosmochim. Acta 58, 1975–1981.

Iveson, A.A., Webster, J.D., Rowe, M.C., Neill, O.K., 2019. Fluid-melt trace-element partitioning behaviour between evolved melts and aqueous fluids: Experimental constraints on the magmatic-hydrothermal transport of metals. Chem. Geol. 516, 18–41. https://doi.org/10.1016/j.chemgeo.2019.03.029.

John, S.G., 2012. Optimizing sample and spike concentrations for isotopic analysis by double-spike ICPMS. J. Anal. At. Spectrom. 27 (12), 2123–2131. https://doi.org/10.1039/c2ja30215b.

König, S., Wille, M., Voegelin, A., Schoenberg, R., 2016. Molybdenum isotope systematics in subduction zones. Earth Planet. Sci. Lett. 447, 95–102. https://doi.org/10.1016/j.epsl.2016.04.033.

Kunz, M., Xirouchakis, D., Lindsley, D.H., Hausermann, D., 1996. High-pressure phase transition in titanite (CaTiOSiO₄). Am. Mineral. 81 (11–12), 1527–1530. https://doi.org/10.2138/am-1996-11-1225.

Leuthold, J., Müntener, O., Baumgartner, L.P., Putlitz, B., Ovtcharova, M., Schaltegger, U., 2012. Time resolved construction of a bimodal laccolith (Torres del Paine, Patagonia). Earth Planet. Sci. Lett. 325–326, 85–92. https://doi.org/10.1016/j.epsl.2012.01.032.

Leuthold, J., Müntener, O., Baumgartner, L.P., Putlitz, B., Chiaradia, M., 2013. A detailed geochemical study of a shallow arc-related laccolith; the Torres del Paine Mafic complex (Patagonia). J. Petrol. 54 (2), 273–303. https://doi.org/10.1093/petrology/egs069.

Leuthold, J., Müntener, O., Baumgartner, L.P., Putlitz, B., 2014. Petrological constraints on the recycling of mafic crystal mushes and intrusion of braided sills in the Torres del Paine Mafic complex (Patagonia). J. Petrol. 55 (5), 917–949. https://doi.org/10.1093/petrology/egu011.

Li, Y., McCoy-West, A.J., Zhang, S., Selby, D., Burton, K.W., Horan, K., 2019. Controlling mechanisms for molybdenum isotope fractionation in porphyry deposits: the Qulong example. Econ. Geol. 114 (5), 981–992. https://doi.org/10.5382/econgeo.4653.

Mathur, R., Brantley, S., Anbar, A., Munizaga, F., Maksaev, V., Newberry, R., Vervoort, J., Hart, G., 2010. Variation of Mo isotopes from molybdenite in high-temperature hydrothermal ore deposits. Mineral. Deposita 45 (1), 43–50. https://doi.org/10.1007/s00126-009-0257-z.

McManus, J., Nägler, T.F., Siebert, C., Wheat, C.G., Hammond, D.E., 2002. Oceanic molybdenum isotope fractionation: Diagenesis and hydrothermal ridge-flank alteration. Geochem. Geophys. Geosyst. 3 (12), 1–9. https://doi.org/10.1029/2002gc000356.

Michael, P.J., 1984. Chemical differentiation of the Cordillera Paine granite (southern Chile) by in situ fractional crystallization. Contrib. Mineral. Petrol. 87 (2), 179–195. https://doi.org/10.1007/bf00376223.

Michael, P.J., 1991. Intrusion of basaltic magma into a crystallizing granitic magma chamber: the Cordillera del Paine pluton in southern Chile. Contrib. Mineral. Petrol. 108 (4), 396–418. https://doi.org/10.1007/bf00303446.

Michel, J., Baumgartner, L., Putlitz, B., Schaltegger, U., Ovtcharova, M., 2008. Incremental growth of the Patagonian Torres del Paine laccolith over 90 k.y. Geology 36 (6), 459–462. https://doi.org/10.1130/g24546a.1.

Müntener, O., Ewing, T., Baumgartner, L.P., Manzini, M., Roux, T., Pellaud, P., Allemann, L., 2018. Source and fractionation controls on subduction-related plutons and dike swarms in southern Patagonia (Torres del Paine area) and the low Nb/Ta of upper crustal igneous rocks. Contrib. Mineral. Petrol. 173 (5), 1–22. https://doi.org/10.1007/s00410-018-1467-0.

Nägler, T.F., Siebert, C., Lüschen, H., Böttcher, M.E., 2005. Sedimentary Mo isotope record across the Holocene fresh-brackish water transition of the Black Sea. Chem. Geol. 219 (1–4), 283–295. https://doi.org/10.1016/j.chemgeo.2005.03.006.

O'Neill, H.S.C., Eggins, S.M., 2002. The effect of melt composition on trace element partitioning: an experimental investigation of the activity coefficients of FeO, NiO, CoO, MoO_2 and MoO_3 in silicate melts. Chem. Geol. 186, 151–181. https://doi.org/10.1016/S0009-2541(01)00414-4.

Pettke, T., Oberli, F., Audétat, A., Guillong, M., Simon, A.C., Hanley, J.J., Klemm, L.M., 2012. Recent developments in element concentration and isotope ratio analysis of individual fluid inclusions by laser ablation single and multiple collector ICP-MS. Ore Geol. Rev. 44, 10–38. https://doi.org/10.1016/j.oregeorev.2011.11.001.

Ramírez de Arellano, C., Putlitz, B., Müntener, O., Ovtcharova, M., 2012. High precision U/Pb zircon dating of the Chaltén Plutonic complex (Cerro Fitz Roy, Patagonia) and its relationship to arc migration in the southernmost Andes. Tectonics 31 (4), TC4009. https://doi.org/10.1029/2011TC003048.

Rempel, K.U., Williams-Jones, A.E., Migdisov, A.A., 2008. The solubility of molybdenum dioxide and trioxide in HCl-bearing water vapour at 350 °C and pressures up to 160 bars. Geochim. Cosmochim. Acta 72, 3074–3083. https://doi.org/10.1016/j.gca.2008.04.015.

Rempel, K.U., Williams-Jones, A.E., Migdisov, A.A., 2009. The partitioning of molybdenum(VI) between aqueous liquid and vapour at temperatures up to 370 °C. Geochim. Cosmochim. Acta 73 (11), 3381–3392. https://doi.org/10.1016/j.gca.2009.03.004.

Rudge, J.F., Reynolds, B.C., Bourdon, B., 2009. The double spike toolbox. Chem. Geol. 265 (3–4), 420–431. https://doi.org/10.1016/j.chemgeo.2009.05.010.

Shafiei, B., Shamanian, G., Mathur, R., Mirnejad, H., 2015. Mo isotope fractionation during hydrothermal evolution of porphyry Cu systems. Mineral. Deposita 50 (3), 281–291. https://doi.org/10.1007/s00126-014-0537-0.

Shannon, B., 1976. Revised effective ionic radii and systematic studies of interatomic distances in halides and chalcogenides. *Acta Crystallographica*, A 32, 751–767.

Siebert, C., Nägler, T.F., Kramers, J.D., 2001. Determination of molybdenum isotope fractionation by double-spike multicollector inductively coupled plasma mass spectrometry. Geochem. Geophys. Geosyst. 2 (7) https://doi.org/10.1029/2000gc000124, 2000GC000124.

Siebert, C., Nägler, T.F., von Blanckenburg, F., Kramers, J.D., 2003. Molybdenum isotope records as a potential new proxy for paleoceanography. Earth Planet. Sci. Lett. 211, 159–171. https://doi.org/10.1016/S0012-821X(03)00189-4.

Siebert, C., McManus, J., Bice, A., Poulson, R., Berelson, W.M., 2006. Molybdenum isotope signatures in continental margin marine sediments. Earth Planet. Sci. Lett. 241 (3–4), 723–733. https://doi.org/10.1016/j.epsl.2005.11.010.

Tattitch, B.C., Blundy, J.D., 2017. Cu-Mo partitioning between felsic melts and saline-aqueous fluids as a function of X-NaCleq, $f(O_2)$, and $f(S_2)$. Am. Mineral. 102, 1987–2006. https://doi.org/10.2138/am-2017-5998.

Ulrich, T., Mavrogenes, J., 2008. An experimental study of the solubility of molybdenum in H_2O and KCl–H_2O solutions from 500 °C to 800 °C, and 150 to 300 MPa. Geochim. Cosmochim. Acta 72, 2316–2330. https://doi.org/10.1016/j.gca.2008.02.014.

Villalobos-Orchard, J., Freymuth, H., O'Driscoll, B., Elliott, T., Williams, H., Casalini, M., Willbold, M., 2020. Molybdenum isotope ratios in Izu arc basalts: the control of subduction zone fluids on compositional variations in arc volcanic systems. Geochim. Cosmochim. Acta 288, 68–82. https://doi.org/10.1016/j.gca.2020.07.043.

Voegelin, A.R., Pettke, T., Greber, N.D., von Niederhausern, B., Nägler, T.F., 2014. Magma differentiation fractionates Mo isotope ratios: evidence from the Kos Plateau Tuff (Aegean Arc). Lithos 190, 440–448. https://doi.org/10.1016/j.lithos.2013.12.016.

Whitney, D.L., Evans, B.W., 2010. Abbreviations for names of rock-forming minerals. Am. Mineral. 95 (1), 185–187. https://doi.org/10.2138/am.2010.3371.

Willbold, M., Elliott, T., 2017. Molybdenum isotope variations in magmatic rocks. Chem. Geol. 449, 253–268. https://doi.org/10.1016/j.chemgeo.2016.12.011.

Willbold, M., Hibbert, K., Lai, Y.J., Freymuth, H., Hin, R.C., Coath, C., Vils, F., Elliott, T., 2016. High-precision mass-dependent molybdenum isotope variations in magmatic rocks determined by double-spike MC-ICP-MS. Geostand. Geoanal. Res. 40 (3), 389–403. https://doi.org/10.1111/j.1751-908X.2015.00388.x.

Wille, M., Kramers, J.D., Nägler, T.F., Beukes, N.J., Schröder, S., Meisel, T., Lacassie, J.P., Voegelin, A.R., 2007. Evidence for a gradual rise of oxygen between 2.6 and 2.5 Ga from Mo isotopes and Re-PGE signatures in shales. Geochim. Cosmochim. Acta 71 (10), 2417–2435. https://doi.org/10.1016/j.gca.2007.02.019.

Wille, M., Nebel, O., Pettke, T., Vroon, P.Z., König, S., Schoenberg, R., 2018. Molybdenum isotope variations in calc-alkaline lavas from the Banda arc, Indonesia: Assessing the effect of crystal fractionation in creating isotopically heavy continental crust. Chem. Geol. 485, 1–13. https://doi.org/10.1016/j.chemgeo.2018.02.037.

Wilson, T.J., 1991. Transition from back-arc to foreland basin development in the southernmost Andes - stratigraphic record from the Ultima-Esperanza-District, Chile. Geol. Soc. Am. Bull. 103 (1), 98–111. https://doi.org/10.1130/0016-7606(1991)103<0098:tfbatf>2.3.co;2.

Yang, J., Siebert, C., Barling, J., Savage, P., Liang, Y.H., Halliday, A.N., 2015. Absence of molybdenum isotope fractionation during magmatic differentiation at Hekla

volcano, Iceland. Geochim. Cosmochim. Acta 162, 126–136. https://doi.org/10.1016/j.gca.2015.04.011.

Yang, J., Barling, J., Siebert, C., Fietzke, J., Stephens, E., Halliday, A.N., 2017. The molybdenum isotopic compositions of I-, S-and A-type granitic suites. Geochim. Cosmochim. Acta 205, 168–186. https://doi.org/10.1016/j.gca.2017.01.027.

Young, E.D., Manning, C.E., Schauble, E.A., Shahar, A., Macris, C.A., Lazar, C., Jordan, M., 2015. High-temperature equilibrium isotope fractionation of non-traditional stable isotopes: experiments, theory, and applications. Chem. Geol. 395, 176–195. https://doi.org/10.1016/j.chemgeo.2014.12.013.

Zack, T., Kronz, A., Foley, S.F., Rivers, T., 2002. Trace element abundances in rutiles from eclogites and associated garnet mica schists. Chem. Geol. 184 (1–2), 97–122. https://doi.org/10.1016/S0009-2541(01)00357-6.

Zajacz, Z., Halter, W.E., Pettke, T., Guillong, M., 2008. Determination of fluid/melt partition coefficients by LA-ICPMS analysis of co-existing fluid and silicate melt inclusions: Controls on element partitioning. Geochim. Cosmochim. Acta 72 (8), 2169–2197. https://doi.org/10.1016/j.gca.2008.01.034.